Available online at www.sciencedirect.com
SCIENCE DIRECT®
Journal of volcanology and geothermal research
ELSEVIER
Journal of Volcanology and Geothermal Research 149 (2006) 1–46
www.elsevier.com/locate/jvolgeores

View of an intact oceanic arc, from surficial to mesozonal levels: Cretaceous Alisitos arc, Baja California

Cathy Busby [a,*], Benjamin Fackler Adams [b], James Mattinson [c], Stephen Deoreo [d]

[a] *Department of Geological Sciences, University of California, Santa Barbara CA 93101, USA*
[b] *Interdisciplinary Sciences, Skagit Valley College, 2405 E College Way, Mt Vernon, WA 98273, USA*
[c] *Department of Geological Sciences, University of California, Santa Barbara CA 93101, USA*
[d] *Department of Geological Sciences, University of California, Santa Barbara, CA 93106, USA*

Received 29 January 2005; received in revised form 13 June 2005; accepted 19 June 2005

Abstract

The Alisitos arc is an approximately 300 × 30 km oceanic arc terrane that lies in the western wall of the Peninsular Ranges batholith south of the modern Agua Blanca fault zone in Baja California. We have completed detailed mapping and dating of a 50 × 30 km segment of this terrane in the El Rosario to Mission San Fernando areas, as well as reconnaissance mapping and dating in the next 50 × 30 km segment to the north, in the San Quintin area. We recognize two evolutionary phases in this part of the arc terrane: (I) extensional oceanic arc, characterized by intermediate to silicic explosive and effusive volcanism, culminating in caldera-forming silicic ignimbrite eruptions at the onset of arc rifting, and (II) rifted oceanic arc, characterized by mafic effusive and hydroclastic rocks and abundant dike swarms. Two types of units are widespread enough to permit tentative stratigraphic correlation across much of this 100-km-long segment of the arc: a welded dacite ignimbrite (tuff of Aguajito), and a deepwater debris-avalanche deposit. New U–Pb zircon data from the volcanic and plutonic rocks of both phases indicate that the entire 4000-m-thick section accumulated in about 1.5 MY, at 111–110 MY. Southwestern North American sources for two zircon grains with Proterozoic $^{206}Pb/^{207}Pb$ ages support the interpretation that the oceanic arc fringed North America rather than representing an exotic terrane.

The excellent preservation and exposure of the Alistos arc terrane makes it ideal for three-dimensional study of the structural, stratigraphic and intrusive history of an oceanic arc terrane. The segment mapped and dated in detail has a central major subaerial edifice, flanked by a down-faulted deepwater marine basin to the north, and a volcano-bounded shallow-water marine basin to the south. The rugged down-faulted flank of the edifice produced mass wasting, plumbed large-volume eruptions to the surface, and caused pyroclastic flows to disintegrate into turbulent suspensions that mixed completely with water. In contrast, gentler slopes on the opposite flank allowed pyroclastic flows to enter the sea with integrity, and supported extensive buildups of bioherms. Caldera collapse on the major subaerial edifice ponded the tuff of Aguajito to a thickness of at least 3 km. The outflow ignimbrite forms a marker in nonmarine to shallow marine sections, and in deepwater sections it occurs as blocks up to 150 m long in a debris-avalanche deposit. These welded ignimbrite blocks were deposited hot enough to deform

* Corresponding author. Tel.: +1 805 893 3471.
E-mail address: busby@geol.ucsb.edu (C. Busby).

0377-0273/$ - see front matter
doi:10.1016/j.jvolgeores.2005.06.009

plastically and form peperite with the debris-avalanche matrix. The debris avalanche was likely triggered by injection of feeder dikes along the basin-bounding fault zone during the caldera-forming eruption.

Intra-arc extension controlled very high subsidence rates, followed shortly thereafter by accretion through back-arc basin closure by 105 Ma. Accretion of the oceanic arc may have been accomplished by detachment of the upper crust along a still hot, thick middle crustal tonalitic layer, during subduction of mafic–ultramafic substrate.

Keywords: oceanic arc; geology; petrography; lithofacies; tectonostratigraphy; U–Pb zircon dating; Alisitos arc; Baja California

1. Introduction

Recent years have seen major advances in understanding of the tectonic, volcanic and sedimentary character of modern oceanic arc systems, through the use of swath-mapping sonar surveys, submersible studies, magnetic and seismic surveys, dredging, and DSDP/ODP coring (e.g., Bloomer et al., 1989; Taylor et al., 1990, 1991; Nishimura et al., 1992; Klaus et al., 1992; Taylor, 1992; Cambray et al., 1995; Clift and ODP Leg 135 Scientific Party, 1995; Fiske et al., 1995; Kokelaar and Romagnoli, 1995; Yuasa, 1995; Fryer, 1996; Murakami, 1996; Wright, 1996; Clift and Lee, 1998; Fryer et al., 1998; Takahashi et al., 1998; Yamazaki and Murakami, 1998; Izasa et al., 1999; Wright and Gamble, 1999; Worthington et al., 1999; Glasby et al., 2000; Bloomer et al., 2001; Wright et al., 2003; Yuasa and Kano, 2003). These studies give a largely two-dimensional view of oceanic arcs. Drill holes and geophysical studies yield some insights into the third dimension, but these are widely spaced. For this reason, we targeted a segment of an ancient oceanic arc terrane for detailed three-dimensional outcrop study (Fig. 1). This terrane, the Alisitos arc, provides one of the best exposed and best-preserved outcrop examples of an oceanic arc reported in the literature to date (Fackler Adams and Busby, 1998). The segment we have mapped in detail (Figs. 1–5) contains no postdepositional faults, and subgreenschist metamorphism allows recognition of primary microtextures. This makes it ideal for three-dimensional study of the structural, stratigraphic and intrusive history of an oceanic arc terrane. Our results can be used to extrapolate into the third dimension, with greater detail, than is possible using the limited sample base of modern oceanic arc systems.

The Alisitos arc is a large (approximately 300×30 km) oceanic arc terrane that lies in the western wall of the Peninsular Ranges batholith in Baja California, south of the modern Agua Blanca fault zone (Fig. 1). A full discussion of the geologic setting of this oceanic arc terrane is given by Busby (2004). Geochemical and isotopic data support the oceanic arc interpretation, but several different models have been proposed for the numbers and polarities of subduction zones involved in its generation and subsequent accretion to the Mexican continental margin (see references in Busby, 2004). Most models for Mesozoic oceanic arc terranes of western Mexico fall into two broad categories: (1) the exotic arc model, where western Mexico grew through accretion of exotic island arcs by the consumption of entire ocean basins at multiple subduction zones with varying polarities, and (2) the fringing arc model, where extensional processes in the upper plate of an east-dipping subduction zone produced arc-related basins, some rifted off the continental margin and others formed of new oceanic lithosphere that largely lay within reach of North American turbidite fans (Centeno-Garcia, 2005 and pers. comm.). In the fringing arc model, later phases of east-dipping subduction juxtaposed these terranes through transtensional, transpressional or compressional tectonics (Busby, 2004). Preliminary zircon provenance data support the fringing arc model for at least parts of the Alisitos arc (Schmidt et al., 2002; preliminary data presented below). To summarize, we interpret the Alisitos arc to be a oceanic arc that fringed the continental margin along an east-dipping subduction zone; it formed in an extensional strain regime, with well-preserved syndepositional normal faults and high rates of subsidence in both the arc region and the forearc region (Busby, 2004).

In this paper we present the results of detailed (1 : 10,000 scale) mapping, petrographic analysis and dating of a 50×30 km segment of the Alisitos arc ter-

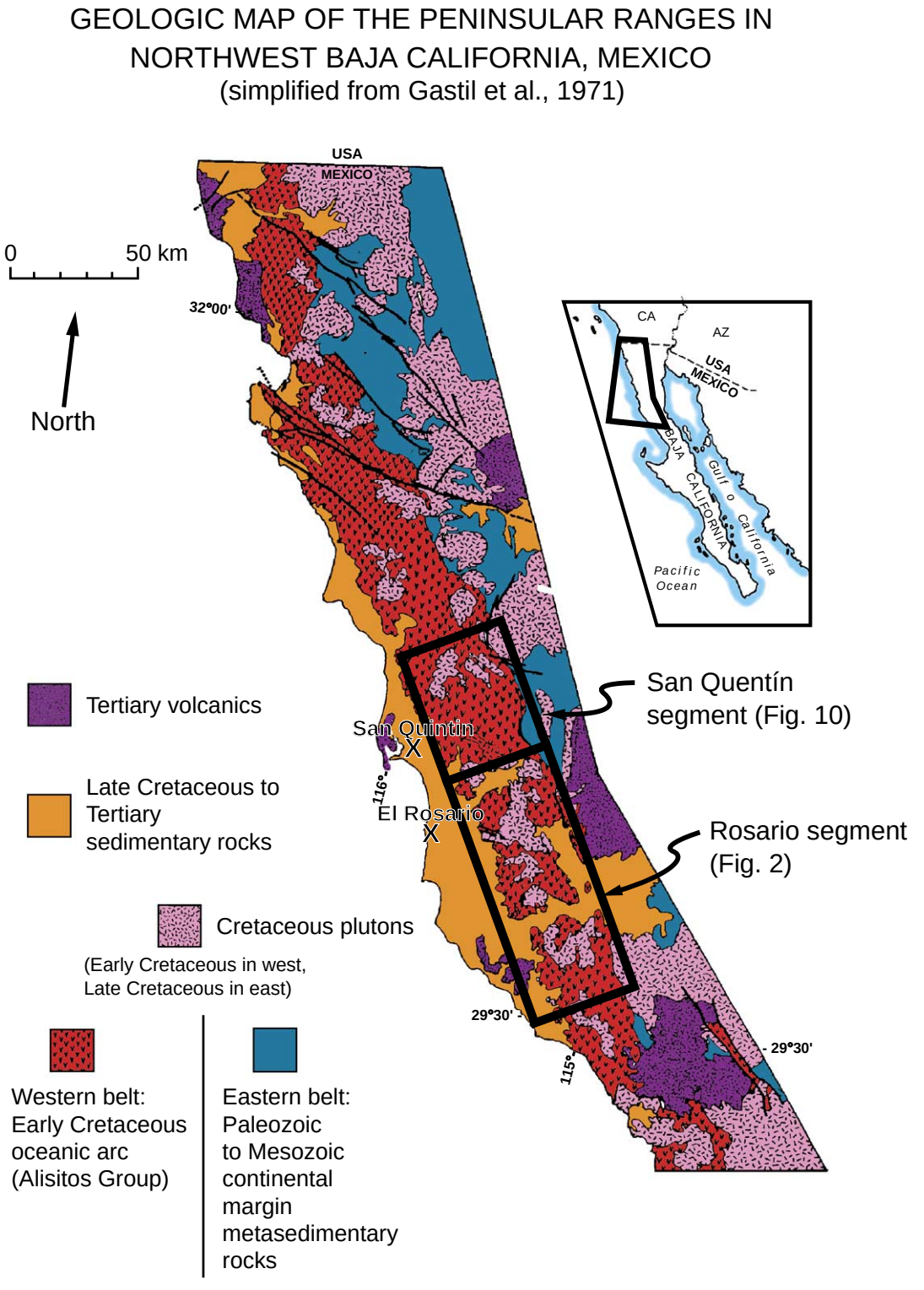

Fig. 1. Geologic setting of the Alisitos arc, western Peninsular Ranges, Baja California, Mexico.

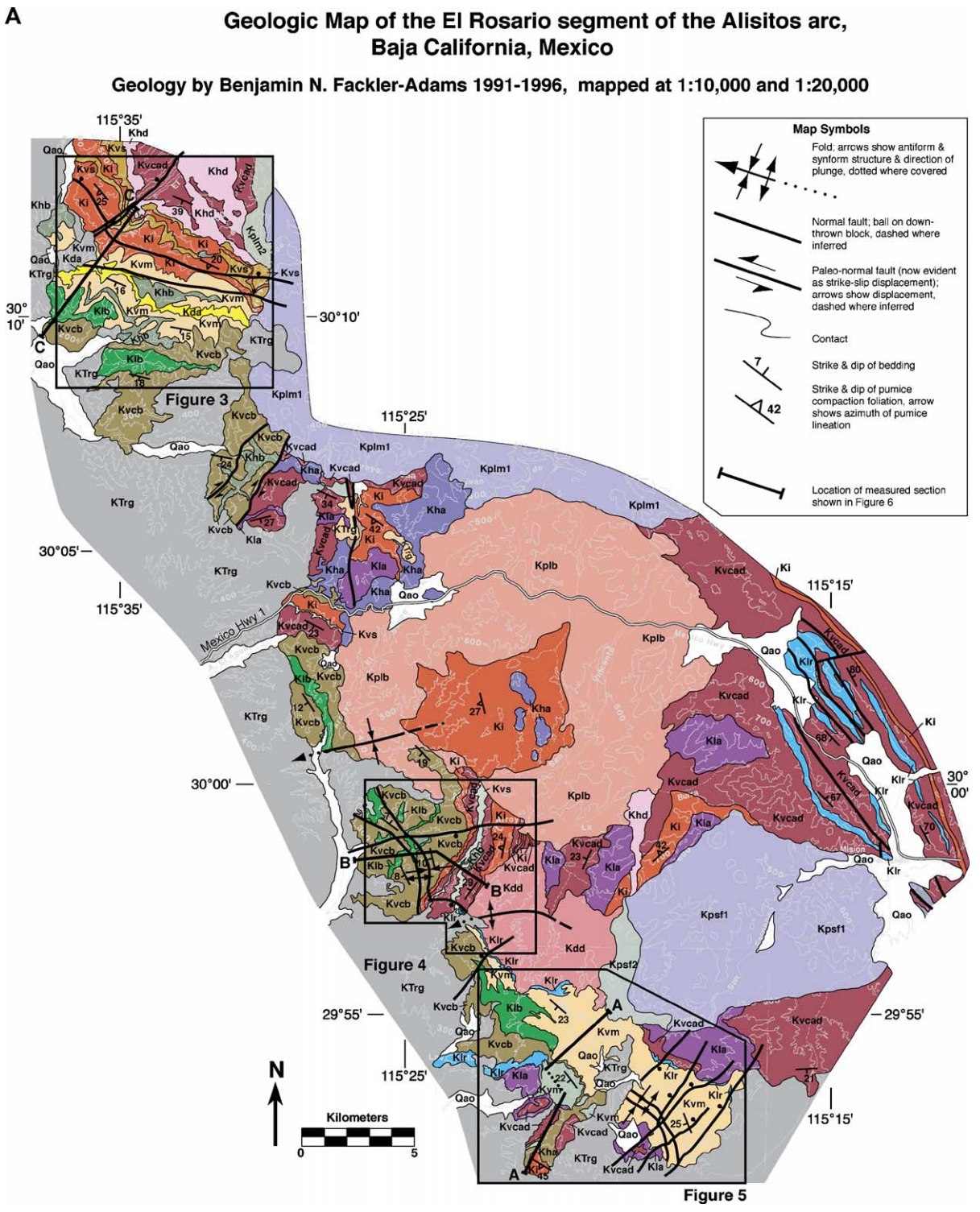

Fig. 2. Geologic map of the Rosario segment of the Alisitos arc (locality shown on Fig. 1).

B Explanation

Qal/Qoa - Alluvium & older alluvium — Quat.

KTrg - Rosario Group - sedimentary rocks, undifferentiated — L. Cret.-Tertiary

Volcaniclastic and Sedimentary Rocks

Kcvad - Dacitic/rhyolitic and andesitic pyroclastic rocks, largely nonmarine
Recessive-weathering, grey to tan & brown outcrops of lithic lapilli tuff, tuff breccia, and breccia in massive, matrix- to clast-supported, very thick- to medium beds. Largely monlithic. Lithofacies include: block-and-ash-flow tuff, pyroclastic surge and fallout deposts, flow breccia and dome talus, gravelly hyperconcentrated flood flow deposits, & lesser debris flow deposits; also includes welded ignibrites not mapped indiviually (see Ki).

Ki - Dacite/rhyolite & andesite welded ignimbrite, nonmarine
Gray to tan resistant outcrops and cliffs in both weathered and fresh exposures. Pumice lapilli tuff & lithic pumice lapilli tuff with eutaxitic textures (pumice flattening 1:3 to 1:20) and sintered glass shards, degassing pipes and basal vitrophyres. Includes lineated high-grade ignimbrites with rheomorphic folds & zone breccias. ontain 5-30% crystals, 30-95% shards, 6-30% pumice, & tr - 5% lithics. Plag >> qtz >> hb, bt, cpx, & opaques. Commonly spherulitically devitrified. Lithofacies include: welded ignimbrite, lesser pyroclastic fallout & pyroclastic surge,

Kda - Debris Avalanche Deposit
Brown-weathering, cliff-forming 100 m thick deposit of blocks and mega-blocks dispersed within a largey massive tuffaceous volcanic sandstone matrix. Megablocks up to 150 m long and 20 m thick are composed of rheomorphic to densely welded ignimbrite (derived from tuff of Aguajito, Figure 4). Ignimbrite blocks commonly show peperitic interaction with host matrix. Massive debris avalanche deposit cotains a few horizons of bedded tuff turbidite. Deeepwater silicic fire fountain deposits occur at the base.

Kvcb - Basaltic volcaniclastic rocks
Green-weathering slope former. Lithic lapilli tuff, tuff breccia and breccia in matrix- to clast-supported, medium to very thick beds. Lithofacies include: Flow breccia, hyaloclastite breccia, coarse-grained tuff turbidite, pillow breccia, gravelly hyperconcentrated flood flow deposits, and fire-fountain deposits.

Kvm - Marine tuffaceous volcaniclastic rocks, including subaqueous pyroclastic flow deposits and tuff turbidites
Tan weathering, well-stratified tuff, tuffaceous sandstone, pumice lapilli tuff & calcareous shale. Bioturbation and marine fossils common . Lithofacies include: mudstone & siltstone; coarse-grained, massive & laminated tuff turbidite; non-welded ignimbrite; pyroclastic fallout;and bioclastic turbidite.

Kvs - Subaerial tuffaceous volcaniclastic rocks
Orange to maroon weathering lithic tuff, lithic lapilli tuff & tuffaceous sandstone in thin to medium tabular & lenticular beds with planar lamination and trough cross lamination, or thick bed with crude lamination. Includes paleosol horizons with mottled textures, reduction spots, & root casts. Lithofacies include: gravelly and sandy hyperconcetrated flood flow deposits and dilute flow deposits; pyroclastic fallout deposits; minor paleosols & debris flow deposits.

Klr - Limestone; bound-, wacke-, & grainstone
Fossiliferous with abundant articulated rudists & rudist fragments, lesser coral, pelycepods, brachiopods, gastropods, & minor ammonites. Lithofacies include: rudist reef, and minor bioclastic turbidites.

Effusive Rocks

Kdd - Dacite/rhyolite lava dome & associated dome talus
Light-colored cliff former. Lava flows are predominantly massive with minor to abundant autobreccia & local flow-banding. Talus is markedly laterally discontinuous, clast- & matrix-supported, & monolithic; locally indistinguishable from brecciated parts of hypabyssal intrusions. Lavas are microporphyritic to coarsely porphyritic, and locally vesicular with 0-12 % qtz, 10-40% plag, 2-5% hb, 1-15% cpx, & 2-7% opaques; remainder is groundmass. Plagioclase phenocrysts to 5mm common. Lithofacies include: dome lavas & talus, with lesser debris flow deposits.

Klb - Basaltic lava flows & flow breccia
Fresh black/dark gray cliffs and weathered orange ledges of coherent lava flow, lesser flow breccia, and minor local pillow lava. Breccias are laterally discontinuous, clast- & matrix-supported, & predominantly basaltic monolithic compositions. Lavas are aphyric to sparsely porphyritic with plag, ol, cpx, & opaques. Flow breccias are laterally discontinuous, clast- & matrix-supported, & monolithic. Lithofacies include: coherent lava flows, flow breccia, with lesser debris flow deposits. In marine sections pillow breccia is a common component with lesser pillow lava.

Kla - Andesite lava flows & flow breccia
Tan resistant outcrops of coherent lava flows and flow breccia, commonly with flow-banding. Breccias are laterally discontinuous, clast- & matrix-supported,monolithic. Aphyric to coarsely porphyritic with up to ~25%plagioclase phenocrysts, lesser cpx, hb & opaques. Lithofacies include: coherent lava flows, flow breccia, with lesser hypabyssal intrusions and debris flow deposits.

Hypabyssal Rocks

Kha - Andesite hypabyssal intrusions
Dikes, sills, small laccoliths, & pods at a range of scales. Can be coherent, columnar jointed, or flow banded. Microporphyritic to holocrystalline. 0-7% qtz, 25-75% plag, 15-20% hb, 5-15% opx, 5-20% cpx, 0-10% ol, 2-10% opaques.

Khb - Basaltic - diabasic hypabyssal intrusions
Dark gray to orange weathering dikes, sills, & irregular pods up to ~50 m wide or thick. Also comprises laccoliths up to ~4 km wide and ~1 km thick. Locally columnar jointed or flow banded. Microporphyritic to holocrystalline. 55-75% plag 10-15% opx, 5-20% cpx, tr ol, 2-10% opaques.

Khd - Dacite/rhyolite hypabyssal Intrusions
Light to dark gray massive outcrops with variable amounts of pink plagioclase phenocrysts. Irregular sills & pods at a range of scales. Porphyritc, holocrystalline, & aphyric. Locally strongly propylitically altered. Locally abundant intrusive & hydrothermal (?) breccia. 5-30% qtz, 20-50% plag, 2-20% hb, tr-10% opx, 5-10% cpx, tr-5% ol, 1-5% opaques.

Plutonic Rocks

Kplb - Granite of La Burra
White to tan holocrystalline rock with local miariolitic cavities & microcrystalline texture. 20-35% qtz, 30-40% plag, 5% bt, 10% hb, 25-35% kspar, 10-15% opx,tr cpx, 1-5% opaques. Pyroxenes have rinds of hb & opaques suggesting xenocrystic origin.

Kplm1- Granodiorite of Los Martirez
Forms tan-orange spheroidally-weathered outcrops & grus. ~12 km diameter pluton with variable composition. Within the map area: holocrystalline, 30-35% qtz, 40-45% plag, 7-10% kspar, 7-10% bt, 10-12% hb,1-2% opx, 1-2% opaques.

Kplm2- Quartz Gabbro of Los Martirez
Forms dark gray jointed outcrops & grus. Occurs as a 1-2 km wide western margin to the ~12 km diameter granodiorite of Los Martirez. Within the map area it is holocrystalline with 10-12% qtz, 60-65% plag, tr kspar, 1-2% opaques.

Kpsf - Quartz Diorite of San Fernando
Composite pluton consisting of: early small gabbro body (Kpsf2), black & megaporphyritic with plagioclase and pyroxene phenocrysts up to 3 cm long in a microcrystalline groundmass, 70-75 % plag, 10% opx, & 10-15% cpx; and a later, more voluminous quartz diorite and lesser tonalite (Kpsf1) grey, holocrystalline and locally porphyritic with 2-15% qtz, 60-70% plag, tr bt, 5-10% kspar, 5-7% opx, 1-5% opaques.

Early Cretaceous

Fig. 2 (*continued*).

rane (Figs. 3–5), referred to here as the Rosario segment (Figs. 1 and 2). Previous mapping of this area was reconnaissance in scale, and mainly divided plutons from volcanic/volcaniclastic rocks (Gastil et al., 1975; Beggs, 1984). We also report on reconnaissance mapping and dating in the next 50 × 30 km segment to the north (Fig. 1), referred to here as the San Quintín segment. Both of these segments form roughly NNW-striking, west-dipping homoclines that expose progressively deeper structural levels of the arc terrane toward the east. The size, unusually good exposure, and excellent preservation of the oceanic arc terrane permits comparison of its stratigraphy, structure and plutonic underpinnings with those of modern oceanic arc systems.

The Rosario segment of the Alisitos arc forms a west-dipping monoclinal section approximately 4000 m thick, intruded by contemporaneous hypabyssal and plutonic rocks (Fackler Adams, 1997; Figs. 2, 6). Lateral and vertical facies changes are far too rapid to allow establishment of formations and members; instead, we use 30 lithofacies "building blocks" to construct facies architectural and structural models (Fackler Adams and Busby, 1998). Petrographic and field characteristics of these lithofacies are presented in detail here for the first time, with process and paleoenvironmental interpretations (Table 1), and discussed briefly in the text. We then use these lithofacies building blocks to reconstruct the tectonstratigraphic and magmatic history of the Rosario segment of the Alisitos arc in a series of four time slices (Fig. 7), defined to elucidate broadly synchronous features and events. These remconstructions are used to divide the tectonstratigraphic and magmatic evolution of this oceanic arc terrane into two phases: (I) extensional oceanic arc, which includes 1–3, and (II) rifted oceanic arc, consisting of time slice 4. We then present new U–Pb zircon data from the volcanic and plutonic rocks of both stages, which show that the entire 4000-m-thick section accumulated in only 1.5 MY, at 111–110 Ma. We infer that intra-arc extension controlled very high subsidence rates, followed shortly thereafter by accretion through backarc basin closure by 105 Ma. Finally, we speculate that accretion of the oceanic arc was accomplished by detachment of the upper crust along a still hot, thick middle crustal tonalitic layer, during subduction of mafic–ultramafic substrate.

The Alisitos arc represents the best exposed, largest intact piece of an oceanic arc terrane that we are aware of. It is therefore possible to reconstruct its structural, stratigraphic and intrusive history in detail. The view presented here will be valuable to oceanographers, whose views of modern arcs are limited to "snapshots" of the present day, with data extrapolated between limited sampling points. The Rosario segment of the Alisitos arc is important for providing a time-integrated view of a rifted oceanic arc.

2. Oceanic arc lithofacies

Lithofacies descriptions proceed from least to most explosive volcanism, and from mafic to felsic compositions within those categories, followed by lithofacies formed from remobilized eruptive products, and last, non-volcanogenic sedimentary rocks (Table 1). In this section, lithofacies names are given in italics for ease of comparison with Table 1. Due to space considerations, many of the references used for lithofacies interpretation are cited in Table 1, and the reader is referred to Busby (2004) for selected outcrop photos. Lithofacies fall into three broad categories: those that occur in both subaerial and marine environments, those that occur only in subaerial environments, and those that occur only in marine environments (Table 1). Lithofacies were mapped individually on aerial photographs at scales of 1 : 10,000 to 1 : 20,000, and transferred to enlarged 1 : 50,000 topographic maps where they are commonly grouped (Figs. 3–5). Lithofacies are also grouped on the generalized measured sections (Fig. 6) and on the time slice cross sections (Fig. 7). The volcaniclastic terminology used in Table 1 and this paper largely follows that of Fisher and Schmincke (1984) and Heiken and Wohletz (1985), and is summarized in data repository item 1.[1] Compositional names are applied using mineral assemblages identified in over 400 thin sections (Table 1). In this paper, we use the term "basalt" or "mafic" to refer to rocks bearing phenocrysts of olivine (± pyroxene, plagioclase); we use the term "andesite" or "intermediate composition" to refer to rocks bearing abundant plagioclase phenocrysts (± pyroxene, hornblende); and we use the term "rhyolite/dacite" or "silicic" to refer to

[1] Data repository item 1, Terminology of pyroclastic rocks.

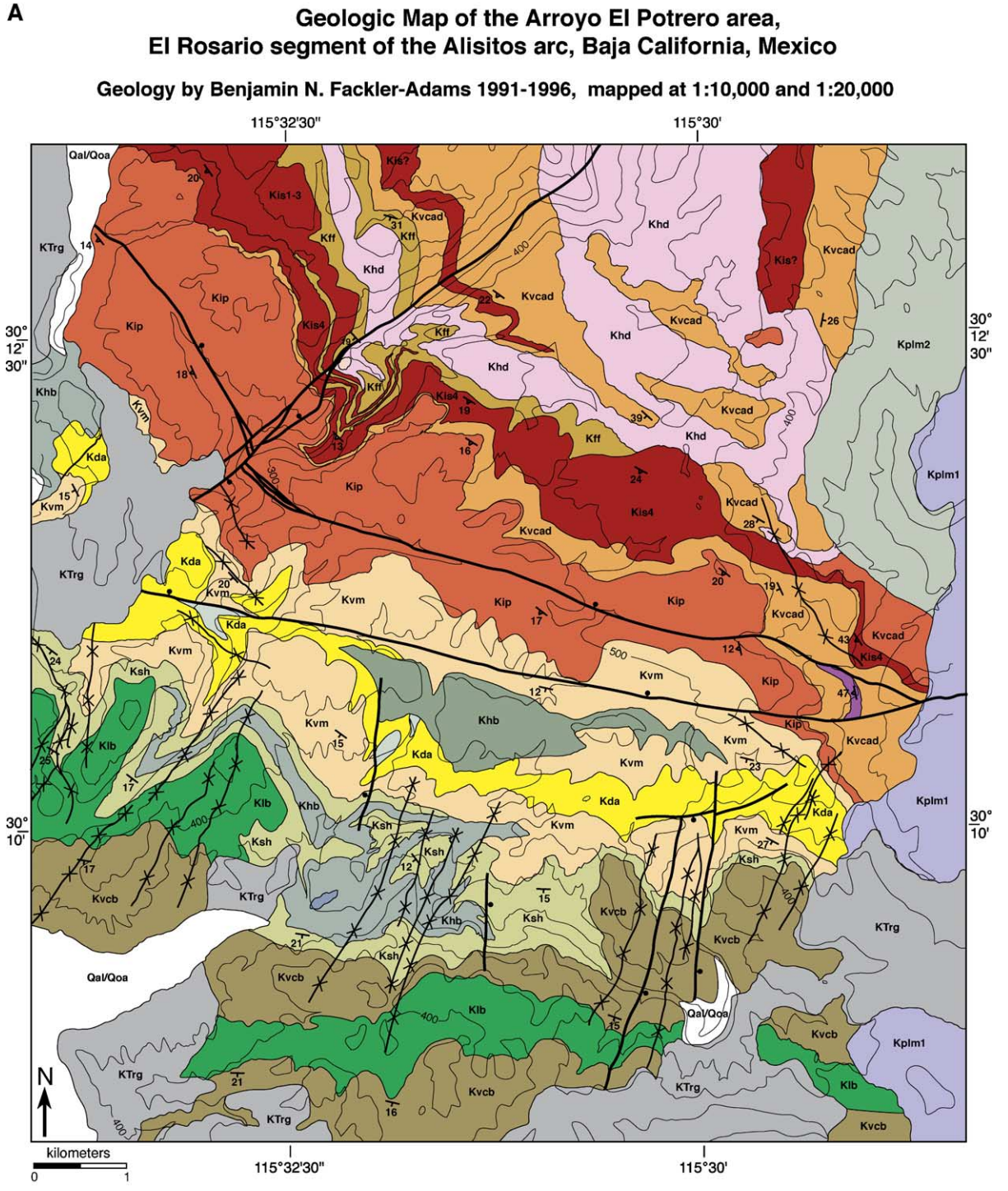

Fig. 3. Geologic map of the Arroyo El Protrero area, northern fault-bounded basin (locality on Fig. 2; generalized stratigraphic section, Fig. 6C).

B Explanation

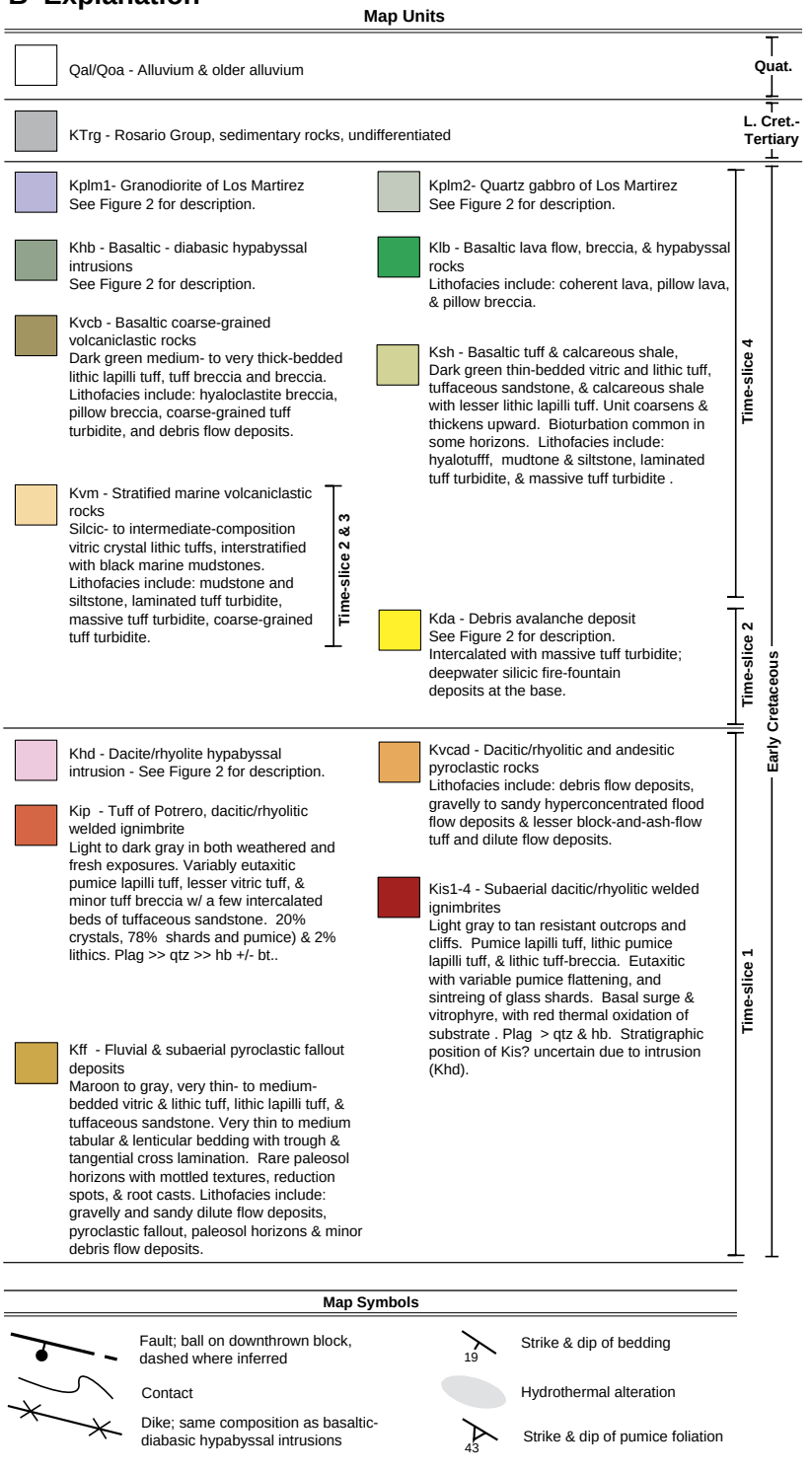

Fig. 3 (*continued*).

rocks bearing phenocrysts of quartz (+plagioclase ± hornblende, pyroxene). Geochemical analysis was beyond the scope of this work, whose goal was to reconstruct the stratigraphic, intrusive and structural evolution of an oceanic arc terrane that was virtually unmapped prior to our study.

2.1. Lithofacies in both subaerial and submarine environments

2.1.1. Effusive volcanic lithofacies

Coherent lava flows (Table 1) are nonbrecciated basaltic and andesitic bodies that are distinguished

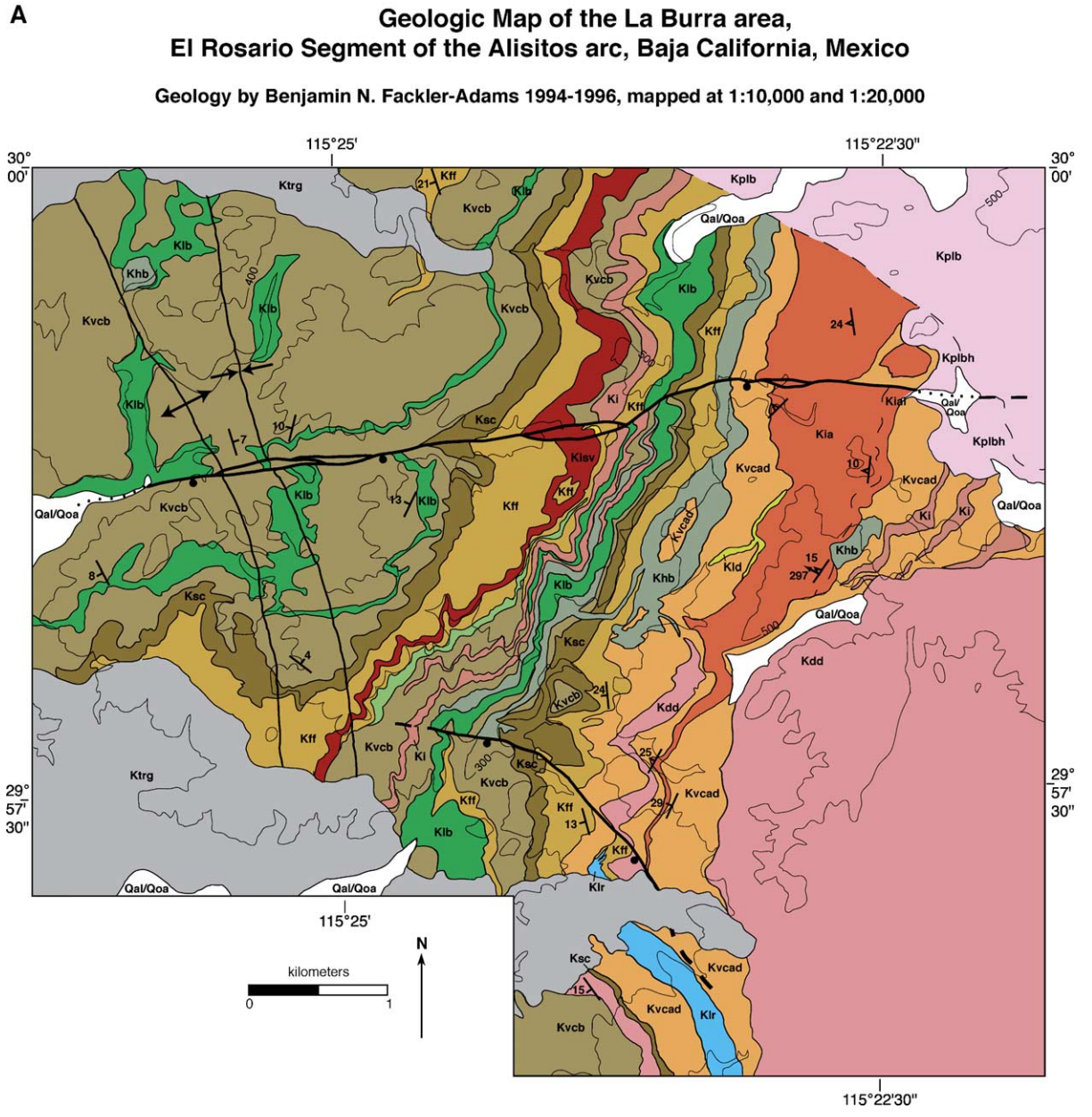

Fig. 4. Geologic map of the La Burra area, showing part of the central subaerial edifice (locality on Fig. 2; generalized stratigraphic section, Fig. 6B).

B Explanation

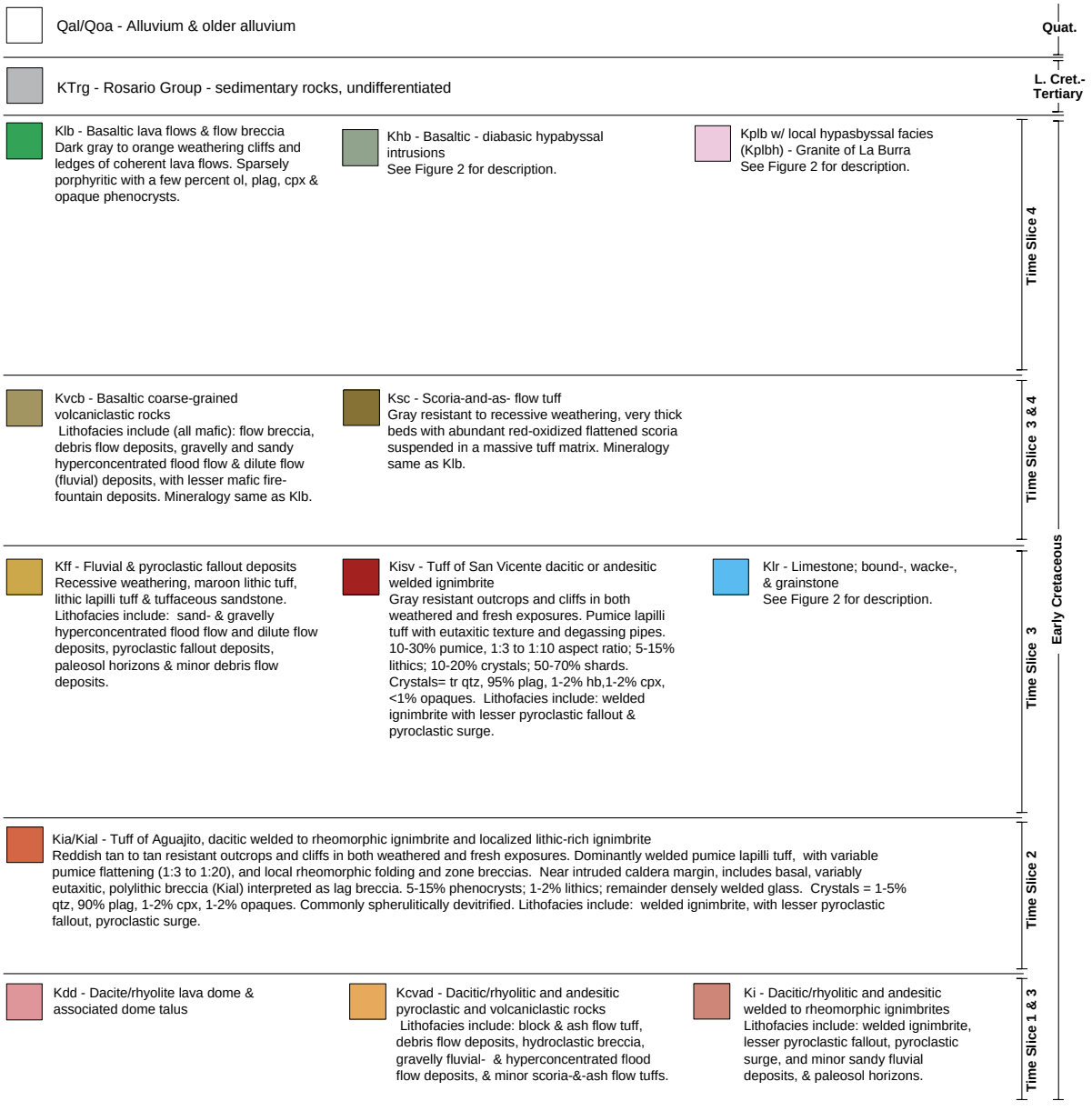

Fig. 4 (*continued*).

from sills by conforming to stratigraphy, containing vesicular tops, and commonly baking underlying strata. Flow breccias are fully to partially autobrecciated basaltic and andesitic lava flows, containing "stony" (nonglassy) aggregates with minimal fine-grained debris. Fire fountain agglomerate consists of accumulations of fluidal basaltic or andesitic clasts as spatter deposits, some with characteristics of post-emplacement flowage. Silicic dome lavas and talus bear quartz phenocrysts and are coherent to brecciated, very thick and laterally discontinuous bodies with large blocks, indicating endogenous dome growth at relatively low extrusion rates (Table 1).

2.1.2. Hyaloclastites and hyalotuffs

Rittman (1962) introduced the term "hyaloclastite" for rocks composed of glass produced by nonexplosive spalling and granulation of pillow rinds, but the term has since been expanded to include all vitroclastic (i.e., glassy) tephra produced by the interaction of water and

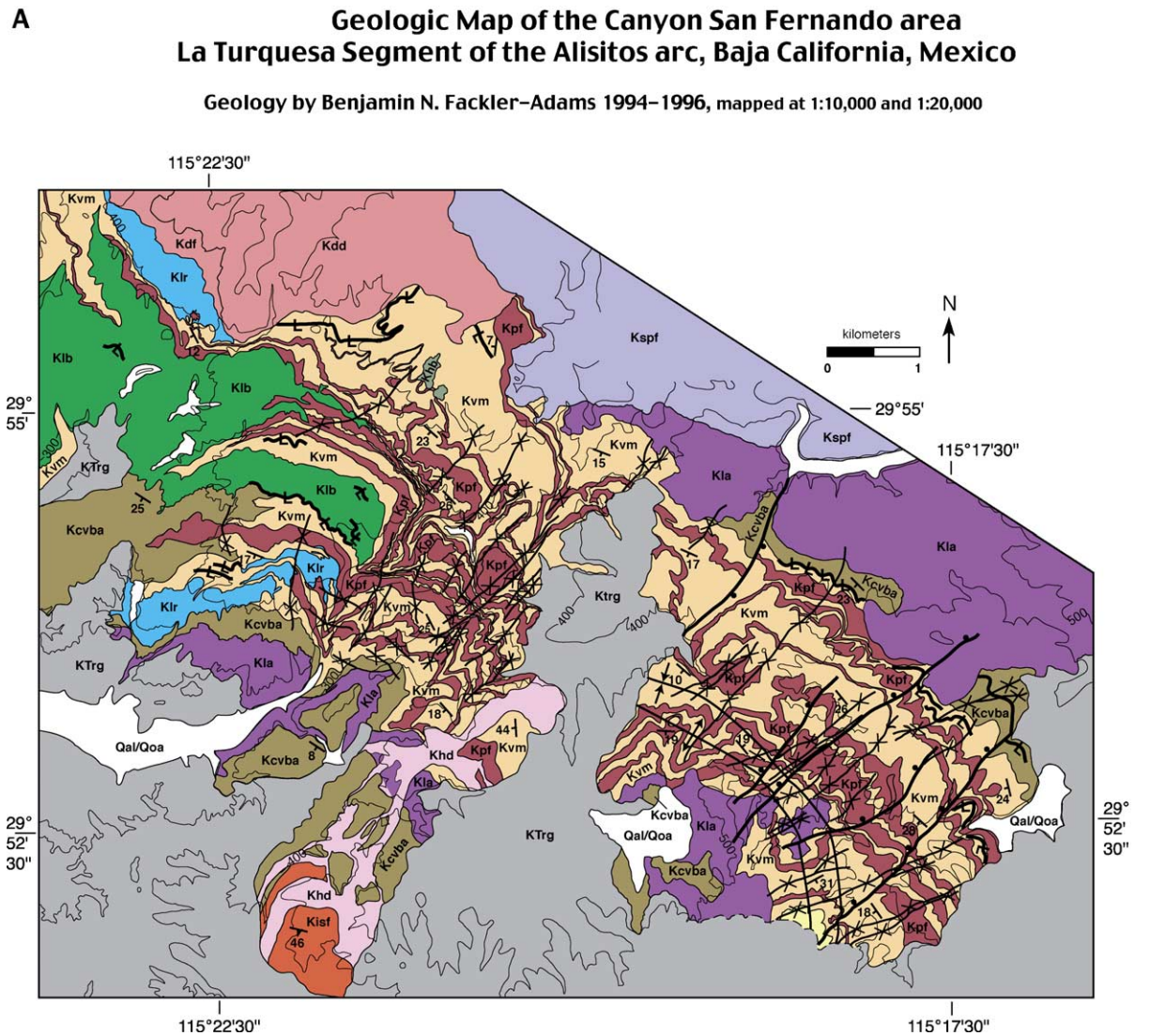

Fig. 5. Geologic map of the Canon San Fernando area, showing the southern volcano-bounded marine basin (locality on Fig. 2; generalized stratigraphic section, Fig. 6A).

B Explanation

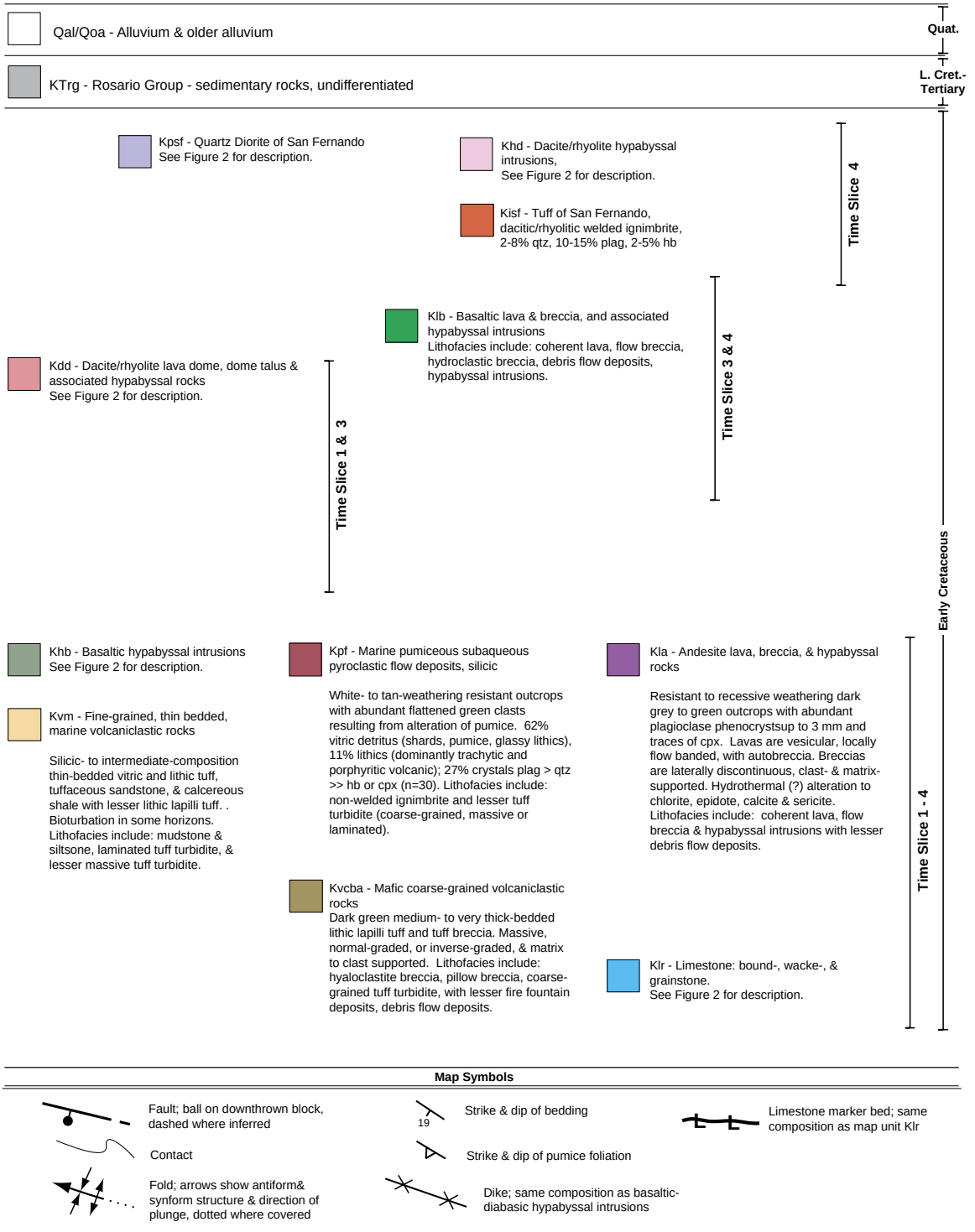

Fig. 5 (*continued*).

hot magma or lava (Fisher and Schmincke, 1984). Other workers restrict the term "hyaloclastite" to the products of non-explosive or mildly explosive quench granulation and use the term "hyalotuff" to describe the products of greater explosivity (Honnorez and Kirst, 1975; Heiken and Wohletz, 1985; Yamagishi, 1987); we follow this useage (Table 1).

Hyaloclastites (Table 1) in the Alisitos arc that formed from sheet lava flows are the "type B" hyaloclastites of Yamagishi (1987); these are much more commonly interstratified with marine strata (Figs. 3, 5) than with nonmarine strata (Fig. 4). Hyaloclastites formed from pillow lavas ("pillow breccia") are restricted to marine environments in the Alisitos arc (described below). Hyalotuffs form thick sections of vitric tuff and lapilli tuff with blocky to bubble-wall glass shard morphology, and monolithic composition (Table 1). In the Alisitos arc, hyalotuffs are restricted to marine paleoenvironments, but in other settings they may form by explosive interaction with groundwater (Fisher and Schmincke, 1984); for this reason, we describe them as lithofacies that may occur in either subaerial or marine environments.

2.1.3. Pyroclastic rocks

Pyroclastic rocks that occur in both subaerial and marine environments (Table 1) include pyroclastic fallout deposits and the following types of pyroclastic flow deposits: block-and-ash-flow tuffs, scoria-and-ash flow tuffs, nonwelded ignimbrites, and welded ignimbrites.

Pyroclastic flow deposits are thick, poorly sorted, massive (nonstratified) deposits of freshly-erupted pyroclastic debris (e.g., glass shards, crystals, pumice and rock fragments), deposited from highly-concentrated pyroclastic density currents (Fisher and Schmincke, 1984; Freundt et al., 2000). Sensu strictu the fluid phase is hot gases, but since the temperature of emplacement can rarely be determined in ancient settings, we use the term sensu lato, i.e., regardless of emplacement temperature (Gibson et al., 2000). Subaqueous pyroclastic flow deposits are the subaqueous equivalent of subaerial pyroclastic flow deposits (Fiske, 1963; Fiske and Matsuda, 1964; Gibson et al., 2000). When pumice-rich pyoclastic flows show evidence for only small to moderate degrees of mixing with water, thereby retaining coherence as highly-concentrated pyroclastic density currents, we refer to them as ignimbrites even though we cannot determine whether the flow was above or below 100 °C at deposition (data repository item 1; Busby-Spera, 1986; Gibson et al., 2000). Where the degree of mixing with water appears to have been great, we refer to them as tuff turbidites (described under "lithofacies only in marine environments", below). Pyroclastic fallout deposits (Table 1) consist of monolithic glass shards, euhedral or broken crystals, and pumice in well-sorted, well-stratified beds that mantle topography. The pyroclastic fallout deposits in marine sections are generally better sorted and stratified than those in nonmarine sections.

Further discussion of pyroclastic terminology is given in repository item 1, and a much more complete description of the subaqueous pyroclastic flow deposits in the Alisitos arc is given in Fackler Adams (1997). For further discussion of the distnguishing features of subaqueous pyroclastic deposits, see White (2000) and Busby (in press).

2.1.4. Remobilized deposits

Remobilized (mass wasting) deposits in the Alisitos oceanic arc are polylithic, composed of a variety of volcanic lithic types. Debris flow deposits (Table 1) are very common and pass gradationally into a variety of other lithofacies including silicic block-and-ash-flow tuff, dome talus, flow breccia, hyaloclastite breccia, and nonwelded ignimbrite. Debris avalanche deposits (Table 1) differ from debris-flow deposits by containing much larger clasts (tens of meters to over a hundred meters in size), within deposits that are much thicker (up to 100 m thick) and much larger in volume (measured in cubic kilometers). Although debris-avalanche deposits may occur in both subaerial and marine environments, in an island arc setting they are far more likely to come to rest in a deep marine environment. A large-volume (>10 km^3) deep marine debris avalanche deposit in the Alisitos arc is described on detail under time slice 3 (below).

2.1.5. Hypabyssal intrusions

Intrusions occur throughout both the subaerial and marine parts of the arc, as dikes, plugs and domes, sills and plutons (Figs. 2–7). In many cases they can be traced directly into extrusive volcanic rocks, and

Table 1
Summary of marine and subaerial lithofacies of the Lower Cretaceous alisitos formation, Baja California, Mexico

Code*	Name	Rock type(s)	Thin section characteristics	Field characteristics	Process and paleoenvironmental interpretations
Subaerial and marine volcanic and volcaniclastic rocks (arranged generally from least to most explosive and from mafic to felsic within those categories)					
Elc	Coherent lava flows	Coherent basalt or andesite lava flows.	Andesite: 10–65% Plag, 1–30% Cpx, 1–7% Opx, 1–5% opaques. Basalt: 1–5% Ol, 2–5% Opx, 1–10% Plag, 1–2% opaques.	Basalt and andesite lava flows are commonly coherent, structureless to flow banded, with rare local columnar jointing. Vesicular bands define flow tops. Conform to stratigraphy and bake underlying strata.	Nonbrecciated lava flows, presumably less viscous/hotter emplacement temperatures than flow breccias.
Efb	Flow breccia	Brecciated basalt or andesite lava flows or parts of lava flows.	Mineralogy as above.	Variably autobrecciated basaltic to andesitic lava flows: coarse, dominantly "stony" (nonglassy) aggregates with minimal fine-grained debris, ranging from complete brecciation to brecciated tops and bases with coherent interiors.	Autobrecciated lava flows formed by mechanical friction during movement of a cooling lava flow.
Eag	Basalt–andesite fire-fountain deposits	Spatter deposits of basalt or andesite.	Mineralogy as above.	Clast-supported monomict breccias with marked molding of clasts against each other. Commonly exhibit internal stratigraphy indicative of post-emplacement flow, including flow folding of fluidal magma rags, and autobrecciation of spatter.	Fire-fountaining of mafic fluidal clasts to produce spatter cones, ramparts, and clastogenic lava flows.
Eld	Silicic dome lavas and talus	Coherent dacite mantled by or interbedded with breccia of the same composition.	Dacites and plagioclase rhyolites: 10–50% Plag, 5–30% Qtz, 5–15% Cpx, 2–20% Hb, 0–10% Opx, 0–5% Bt, 0–5% Ol, 1–5% opaques. Monomict dense (nonvesicular) clasts.	Very thick (10s to 100s of meters) silicic lava flows, with coherent interiors mantled by breccias in gradational, complexly interfingering contact, showing rapid (100s of meters) lateral wedging and decrease in block size away from coherent interiors. Blocks up to 4 m in size.	Extrusion and autobrecciation of viscous silicic lava flows. Lack of extensive lateral flow away from the vent is indicative of endogenic dome growth (Fink and Anderson, 2000). Relatively large block size suggests low extrusion rates (Fink and Anderson, 2000).
Hb	Hyaloclastite breccia	Basaltic or andesitic vitric tuff breccia, breccia, lapillistone and lapilli tuff.	Monolithic, consisting of markedly blocky and cuspate glassy and lesser stony clasts; mineralogy same as basalt or andesite lava flows.	Massive, clast-supported monolithic breccias, containing "stony" (i.e., microlitic) blocks with glassy rims, and glassy lapilli-sized fragments. Glass lapilli show concave–convex outlines and range from equant cubes to angular polyhedrons; blocks have concave–convex irregularities on their surfaces.	Non-explosive or mildly explosive quench granulation of lava flows; lapilli formed by quench granulation and spalling of material off larger blocks, which may in formed in part by flow brecciation. These are the "type B" hyaloclastites of Yamagishi (1987), which consist of polyhedral fragments associated with sheet flows.

Ht	Hyalotuff	Basaltic or andesitic or dacitic vitric tuff.	Monolithic, consisting of markedly blocky and cuspate glass shards and lesser broken crystals; mineralogy same as basalt or andesite or dacite/plagioclase rhyolite (above).	Massive to more commonly well-stratified accumulations of ash-to lapilli-sized glass fragments, in sections meters to tens of meters thick.	Phreatomagmatic eruptions or subaqueous fire fountain eruptions. Thick sections of uniformly comminuted glass record at least mildly explosive eruptions (Honnorez and Kirst, 1975; Heiken and Wohletz, 1985; Yamagishi, 1987). Hyalotuffs are most common in submarine or lacustrine environments but may also form where magmas come into contact with groundwater (Fisher and Schmincke, 1984).
Pb&a	Block-and-ash-flow tuff	Andesitic or dacitic monolithic tuff breccia and lesser lapilli tuff with non-vesiculated clasts.	Monolithic, consisting of dense (nonvesicular) lithic and lesser glassy blocks and lapilli in an ash matrix of the same composition; mineralogy same as rhyolitic, dacitic or andesitic lava flows.	Massive, matrix-supported, in units meters to tens of meters thick. Some clasts exhibit radial jointing and bread-crusted surfaces. Pumice absent.	Hot, gas-fluidized, small-volume blocky pyroclastic flows generated by lava dome collapse (e.g., Fisher et al., 1980; Sparks, 1997; Freundt et al., 2000). Less commonly, block-and-ash flows form by collapse of Vulcanian eruption columns of intermediate composition (Freundt et al., 2000).
Ps&a	Scoria-and-ash-flow tuff	Andesitic or basaltic lapilli tuff with flattened scoria.	Monolithic, consisting of moderately-to well-vesiculated lithic to glassy lapilli and minor blocks dispersed in a coarse ash matrix of the same composition. Mineralogy same as andesitic lava flows.	Massive, matrix-supported, and poorly sorted, in flow units meters to tens of meters thick.	Intermediate to mafic ignimbrites (Fisher and Schmincke, 1984; Freundt et al., 2000), similar to those formed from probable Vulcanian eruptions in the Andean arc (McCurry and Schmidt, 2001), the Aleutian arc (Larsen et al., 2000), the Roman Volcanic province (Giordano et al., 2002), Java (Camus et al., 2000) and the Taupo Volcanic Zone (Wilson et al., 1995).
Pin	Nonwelded ignimbrite	Pumice lapilli tuff with lesser lithic lapilli.	Dominantly monolithic, consisting of pumice lapilli set in a groundmass of vitric tuff with non-sintered bubble-wall shards. Marine nonwelded ignimbrites show perlitic fracture of clasts. Mineralogy same as rhyolitic/dacitic dome lavas.	Abundant pumice, weakly flattened, in an unsorted matrix of crystal vitric tuff; in massive units meters to tens of meters thick, with de-gassing pipes. Subaerial non-welded ignimbrites commonly more lithic-rich than welded ignimbrites. Marine nonwelded ignimbrites are better sorted and stratified, and exhibit steam fluidization of substrate.	Ignimbrites, based on highly pumiceous, massive, poorly sorted nature (Sparks et al., 1973; Fisher and Schmincke, 1984); probably fed by collapse of Plinian eruption columns.

(*continued on next page*)

Table 1 (*continued*)

Code*	Name	Rock type(s)	Thin section characteristics	Field characteristics	Process and paleoenvironmental interpretations
Subaerial and marine volcanic and volcaniclastic rocks (arranged generally from least to most explosive and from mafic to felsic within those categories)					
Piw	Welded ignimbrite	Pumice lapilli tuff and tuff breccia, with highly-flattened pumices.	Dominantly monolithic, consisting of highly flattened pumice lapilli set in a groundmass of vitric tuff with sintered bubble-wall shards. Ultrawelded ignimbrites show extreme plastic deformation of shards and stretching of pumice. Mineralogy same as rhyolitic/dacitic dome lavas.	Ubiquitous eutaxitic texture with vitroplastic flattening of shards, in single and compound cooling units with degassing pipes. Commonly ten's of meters thick; thicker within calderas (500–1000 m), and thinner where pinching out against paleotopography. Locally high-grade, with lineations on planar to highly contorted parting surfaces.	Very hot (≥550 °C), gas-fluidized predominantly pumiceous pyroclastic flows. Includes high-grade ignimbrites, formed by primary deformation of high-temperature pyroclastic flows during transport and deposition (Branney and Kokelaar, 1992; McCurray et al., 1996; Freundt, 1999) or secondary rheomorphic flowage after deposition and deflation (Schmincke and Swanson, 1967; Wolff and Wright, 1981).
Pf	Pyroclastic fallout deposits	Tuff, dust tuff, lapillistone, and lapilli tuff.	Mineralogy varies from that of rhyolite–dacite, andesite and basalt (as above), but each deposit is monolithic, composed of juvenile glass, crystals and juvenile lithic fragments.	Crystal vitric tuff, vitric tuff and nonwelded pumice lapillistone in well sorted and well stratified, thin to very thin beds that mantle topography. Normal and lesser inverse grading common. Subaqueous facies better sorted than subaerial facies.	Subaerial or subaqueous settling of pyroclastic detritus suspended in subaerial or subaqueous eruption-fed pyroclastic clouds. Well-sorted pumice accumulations that mantle topography in thin beds are commonly interpreted as Plinian fall deposits (Fisher and Schmincke, 1984; Houghton et al., 2000a). Exceptionally fine grain size of some subaerial tuffs consistent with Phreatoplinian origin (Self, 1983; Heiken and Wohletz, 1985; Cioni et al., 1992; McPhie et al., 1993; Morissey et al., 2000; Houghton et al., 2000b).
Bda	Debris avalanche deposits	Polylithic volcanic pebbly to bouldery tuffaceous sandstone with very large boulders (1 to 10 m) and megablocks up to 150 m long.	Polylithic volcanic clasts, crystals, shards and bioclastic debris. Large megablocks consist of welded to ultrawelded tuff of Aguajito.	Massive, matrix-supported beds several tens of metres thick, some with graded tops; overall deposit forms a flat-topped sheet. Blocks of high-grade ignimbrite are markedly larger than clasts of other rocks types, and commonly exhibit peperitic contacts with surrounding matrix. Some units contain fluidal and peperitic pebbles and cobbles of high-grade ignimbrite.	"Non-coherent" debris avalanche (e.g., Siebe et al., 1992; Lenat et al., 1989; Wadge et al., 1995; Kerr and Abbott, 1996) with a matrix of soft, fine-grained volcaniclastic and bioclastic materials. Carried megablocks of hot, fluidial high-grade ignimbrite into deep water. Some blocks remained coherent (slide blocks), and others interacted explosively with seawater and surrounding sediment to form fluidal clasts. Very large-scale stratification suggests multiple sedimentation units, perhaps due to retrogressive failure.

Bdf	Debris flow deposits	Polylithic volcanic pebbly to bouldery mudstone and sandstone.	Polylithic volcanic clasts, although matrix commonly exhibits a dominant clast composition (e.g., basaltic or andesitic). Marine deposits commonly contain broken fossils.	Massive, matrix-supported beds 1 meter to a few 10s of meters thick with angular boulder-to pebble-sized clasts. Commonly show no sorting or clast alignment, but may be crudely stratified, with flat clast alignment.	Volcanic mudflows i.e., lahars (definition of Fisher and Schmincke, 1984). The more monolithic varieties may have been eruption fed.
Ih	Hypabyssal intrusions	Dacite, andesite, basalt, diabase, and tonalite.	Dacite/rhyolite: 10–50% Plag., 5–30% Qtz, 2–20% Hb, 5–15% Cpx, tr– 10% Opx, 0–5% Bt, 0–5% Ol, 1–5% opaques. andesite: tr–12% Ol, 2–25% Cpx, 1–30% Opx, 10–95% Plag., 5–10% Hb, 1–5% opaques. Basalt, diabase, and quartz diabase: 0– 10% Ol, 5–20% Cpx, 5–15% Opx, 25–75% Plag., 15–20% Hb, 2–10% opaques. Tonalite 10–15% Cpx, 40–45% Plag., 45–50% Qtz.	Range from phyric microcrystalline to coarsely porphyritic hollocrystalline textures. Some intrusions exhibit peperitic contacts.	Hypabyssal intrusions including sills, dikes, subvolcanic necks, and ring dikes.
Subaerial only volcanic and volcaniclastic rocks (arranged from most to least explosive and from mafic to felsic within those categories)					
Ps	Pyroclastic surge	Crystal vitric tuff, crystal lithic tuff, and lesser crystal tuff.	Crystals dominantly Plag. ± quartz ± minor opaques and altered PX or Hb. Fragments predominantly glassy with lesser trachytic and porphyritic types.	Well sorted, planar-laminated to cross-laminated deposits in lenticular beds less than a meter thick.	Traction sedimentation of pyroclasts from hot, high energy turbulent gas-fluidized flows fed by eruptions.
Gh	Gravelly hyperconcentrated flood flow deposits	Volcanic lithic conglomerate–breccia and pebbly sandstone, lesser tuff & tuffaceous sandstone.	Polylithic and monolithic volcanic pebbles to boulders with volcanic lithic, vitric and crystal sandstone matrix.	Generally clast-supported, massive to lesser crudely laminated, medium to very thick beds filling scours up to 3 m deep. Framework clasts & matrix very poorly sorted and subangular to subrounded.	Fluvial deposits from channel-confined high-concentration flood flows.]Distinguished from gravelly dilute flow deposits by lack of cross stratification, poorer sorting and dominantly massive character.
Subaerial and marine volcanic and volcaniclastic rocks (arranged generally from least to most explosive and from mafic to felsic within those categories)					
Sh	Sandy hyperconcentrated flood flow deposits	Tuffaceous volcanic lithic sandstone with lesser tuffaceous volcanic lithic pebble conglomerate and breccia.	Polymict volcanic lithic, vitric and crystal sandstone. Vitric components typically <20% and altered.	Massive to crudely planar laminated, in thin-bedded tabular sets up to ~15 m thick. Poorly sorted with subangular to subrounded clasts.	Fluvial deposits from nonchannel-confined (i.e., sheetflood) high-concentration flood flows, similar to those described by Smith and Lowe (1991), Collinson (1996), Allen (1997) and Vallance (2000).
Gf	Gravelly dilute flow deposits	Polylithic volcanic breccia–conglomerate and lesser volcanic pebbly sandstone.	Polymict volcanic lithic fragments.	Laminated to cross-laminated, well-sorted clast-supported beds confined to channels up to ~4 m deep. Interstratified tuffaceous sandstone lenses common.	Fluvial deposits from channel-confined dilute flow.

(continued on next page)

Table 1 (*continued*)

Code*	Name	Rock type(s)	Thin section characteristics	Field characteristics	Process and paleoenvironmental interpretations
Subaerial and marine volcanic and volcaniclastic rocks (arranged generally from least to most explosive and from mafic to felsic within those categories)					
Sf	Sandy dilute flow deposits	Tuffaceous volcanic lithic sandstone and lesser volcanic pebble sandstone.	Polylithic volcanic lithic fragments and crystals. Vitric components typically <20% and altered.	Thin-to thick-bedded with planar lamination, trough cross lamination and ripple cross lamination. Moderately well sorted.	Fluvial deposits from nonchannel-confined (i.e., sheetflood) and channelized dilute flow.
Sps	Paleosol horizons	Calcareous, clayey or organic layers	Alteration and local replacement of clasts by clay minerals or calcite nodules.	Massive to patchily stratified, mottled and /or oxidized appearance, sparse root casts.	Poorly developed soil horizons.
Marine only volcanic and volcaniclastic rocks (arranged from most to least explosive and from mafic to felsic within those categories)					
Elp	Pillow lava	Basaltic variably vesicular lobes.	Aphyric to slightly plagioclase phyric basalt. Mineralogysame as basalt lava flows.	Pillows are lensoid bodies with quenched rims, commonly surrounded by hyaloclastite. Locally sparsely vesicular.	Subaqueous flows of low-viscosity basaltic magma. Stacks of well-formed pillows, with keels conforming to the tops of underlying pillows, are very rare; this may indicate that the flows were too viscous to form perfect pillows or that hydroclastic fragmentation was enhanced by extrusion on steep slopes.
Ebp	Pillow breccia	Breccia containing abundant pillow rind clasts, some with peperitic margins against tuffaceous matrix.	Aphyric to slightly plagioclase phyric basalt. Mineralogysame as basalt lava flows.	Massive breccia with abundant pie-shaped pillow fragments and pillow rind fragments, mixed with cuspate and blocky glass fragments. Jig-saw texture locally common.	Quench fragmentation of basaltic pillows during emplacement. These are the "type A" hyaloclastites of Yamagishi, 1987. Pillow breccia is far more common than pillow lavas.
Eag	Deepwater silicic fire fountain deposits	Stratified accumulations of silicic lapilli, blocks and ash, with plastic clast morphologies.	Mineralogy same as rhyolitic/ dacitic lava domes.	Clast-supported beds, some with marked molding of plastic clasts against each other in welded/agglutinated morphologies, others with nonwelded chilled clasts. Plastic clasts Include "cow-pie" (flattened), or amoeboid, or irregularly elongate or twisted clasts. Interstratified with silicic hyalotuff.	Deep marine fire-fountaining of silicic magma to produce fluidal clasts that locally accumulated in a hot enough state to agglutinate. Fluidity of silicic magma may be due to confining pressure of a deep water column, which inhibits exsolution of dissolved volatiles (Cas, 1978; Yamagishi and Dimroth, 1985).
Gb	Beach conglomerate	Conglomerate, well-sorted and well-rounded.	Polylithic volcanic clasts and shell fragments, with minor matrix of calcarenite or volcanic lithic sandstone.	Clast-supported tabular beds with imbricated clasts.	Wave-reworking of volcanic cobbles and pebbles.

Gct	Coarse-grained tuff turbidite	Pumice-and lithic-lapilli tuff and tuff breccia in stratified, graded beds.	Averages 27% crystals, 62% vitric detritus, and 11% volcanic lithic fragments ($n=30$). Euhedral or broken crystals, predominantly Plag. with lesser qtz. and minor Cpx. Vitric detritus includes bubble-wall shards and pumice. Lithics predominantly trachytic and porphyritic, lesser volcaniclastic and plutonic.	Massive to stratified, in matrix-to clast-supported medium to very thick beds.	Traction and suspension sedimentation of pumiceous and volcanic-lithic detritus; analogous to gravelly high-density turbidity current deposits of Lowe (1982).
Smt	Massive tuff turbidite	Tuff and tuffaceous sandstone in dominantly massive graded beds.	Averages 32% euhedral crystals, 31% vitric detritus, 37% volcanic lithic fragments ($n=11$). Components similar to coarse-grained tuff turbidite.	Massive, normally graded, medium to very thick beds.	Traction and suspension sedimentation of sand-grade volcaniclastic detritus; analogous to sandy high-density turbidity current deposits of Lowe (1982).
Sbt	Laminated tuff turbidite	Tuff and tuffaceous sandstone in laminated graded beds.	Averages 28% euhedral crystals, 47% vitric detritus, 25% volcanic lithics ($n=14$).	Planar-laminated, cross-laminated and convolute laminated, normally graded, very thin to medium beds(Bouma Tb, Tc, Td divisions). Locally moderate bioturbation.	Suspension and traction sedimentation of sand-grade volcaniclastic detritus; analogous to the low-density turbidity current deposits of Lowe (1982).
Marine only volcanic and volcaniclastic rocks (arranged from most to least explosive and from mafic to felsic within those categories)					
Fms	Mudstone and siltstone	Interstratified mudstone & siltstone, range from predominantly calcareous to predominantly tuffaceous.	Ranges from micrite with recrystallized microfossils and minor vitric material, to tuffs with up to 12% crystals, 68% vitric detritus, and 20% volcanic lithic fragments ($n=8$).	Very thin to thin bedded, with planar lamination. Lesser Bouma Tcde divisions. Locally partially to completely homogenized by bioturbation.	Suspension sedimentation of biogenic and volcaniclastic detritus from the water column; lesser dilute turbidity current sedimentation.
Biogenic sedimentary rocks (marine only)					
Lr	Rudist reef	Fossiliferous boundstone, wackestone, and lesser grainstone.	Fossils include abundant whole and fragmented rudists, lesser coral, pelycepods, brachiopods, and minor ammonites.	Lensoid bodies, a few to ~10 m thick, that pinch out over a few hundred meters laterally. Lenses may be stacked and shingled.	Accumulation of biogenic detritus to produce a bioherm with positive topographic expression. Growth results from the in situ growth of organisms (dominantly rudists) and by trapping of biogenic and volcaniclastic detritus between the organisms.
Lbt	Bioclastic turbidite	Grainstone, wackestone, and volcanic calcarenite.	Fossiliferous with variable amounts of volcaniclastic detritus.	Clast-to matrix-supported tabular beds, thin to thick bedded, commonly planar laminated and ripple-cross laminated. Bouma Tace, Tbcd, & Tcde. Resistant grey ledge-formers.	Sedimentation of sand-grade reef-derived bioclastic detritus from low-density and high-density turbidity currents.

* Lithofacies code symbols are defined as follows: E — effusive, H — hydroclastic, P — pyroclastic, B — breccia, I — intrusive, G — gravel, S — sandstone, F — fine-grained, L — limestone.

can be grouped with them mineralogically. Those we have dated are the same age as the volcanic rocks (discussed further below). They include dacite, andesite, basalt, diabase and quartz diabase, with microcrystalline to coarsely porphyritic and holocrystalline textures (Table 1).

2.2. Lithofacies only in subaerial environments

The lithofacies that are restricted to the subaerial environment largely reflect the work of running water. Only one type of pyroclastic rock appears to be restricted to the subaerial environment, and that is pyroclastic surge deposits (Table 1). Unlike pyroclastic flows, pyroclastic surges are too dilute and turbulent to flow beneath water and retain any of the characteristics produced on land. Fluvial volcaniclastic rocks show evidence of working by running water, in the form of sorting, lamination and cross lamination, cut and fill structures, and clast imbrication, They are made of subangular to subrounded volcanic rock fragments (monomict to polymict), with variable admixtures of volcanic ash in the form of euhedral crystals, glass shards, pumice and scoria (i.e., tuffaceous sandstone or breccia–conglomerate). Hyperconcentrated flood flow deposits (both gravelly and sandy) are more massive and poorly sorted than dilute flow deposits (both sandy and gravelly), which show abundant lamination and cross lamination (Smith and Lowe, 1991). Hyperconcentrated flood flow deposits are much more common than dilute flow deposits because of (1) episodic, very high sediment supply produced by explosive eruptions, and (2) short, steep fluvial drainage systems on an island arc volcano. Paleosol horizons (Table 1) occur rarely in the Alisitos oceanic arc. This is consistent with the interpretation (discussed below) that tectonic subsidence rates were very high, causing rapid burial of sediments.

2.3. Lithofacies only in marine environments

Primary volcanic rocks that are diagnostic of a marine environment of deposition in the oceanic arc include pillow lava, pillow breccia, and deepwater silicic fire fountain deposits (Table 1). Pillow lavas are very rare in the Alisitos arc relative to pillow breccias and interstratified hyaloclastite breccias, suggesting that hydroclastic fragmentation was in general enhanced by extrusion on steep slopes. Deepwater silicic fire fountain deposits consist largely of nonvesiculated, plastic clasts that are commonly agglutinated (Table 1), suggesting a fire fountain style of eruption rather than a more violent eruption, which would produce well-vesiculated fragments (Mueller and White, 1992; White et al., 2003). These deposits are puzzling, because silicic magmas are generally considered to be too viscous to fountain or exhibit other fluidal behaviors. The fluidity of deepwater rhyolites has been attributed to confining pressure of the water column, which inhibits exsolution of dissolved volatiles, resulting in lower magma viscosity (Cas, 1978; Yamagishi and Dimroth, 1985). This effect is much greater in silicic magmas than it is in mafic magmas (McBirney and Murase, 1984; Bridges, 1997), leading Bridges (1997) to suggest that Venusian volcanic landforms with fluidal features (formed at 90 bars) are silicic lava flows. On Earth, fluidal clast morphologies are commonly reported around mafic submarine volcanoes but none of these examples show clast agglutination (Smith and Batiza, 1989; Gill et al., 1990; Wright, 1996; Clague et al., 2000; Simpson and McPhie, 2001; Fujibayashi and Sakai, 2003; Cas et al., 2003). However, clast agglutination has been described from other silicic submarine volcanic centers (Mueller and White, 1992; Busby, in press). We agree with Mueller and White (1992) that silicic clasts with welded/agglutinated morphologies presumably required insulation of the fire fountain from surrounding water within a cupola of steam, whereas nonwelded plastic clast accumulations with chilled rims probably formed in contact with water.

Pyroclastic deposits restricted to the marine setting are those that show features typical of low- and high-density turbidity current deposits, and are referred to as the tuff turbidite lithofacies. The tuff turbidite lithofacies is composed largely of delicate pyroclastic material, and each bed has a restricted range of mineral types (Table 1); therefore, most of these likely represent eruption-fed turbidity currents, rather than resedimented material, which should be more polymict and abraded. The sedimentary structures closely resemble that of siliciclastic turbidites, however, indicating that liquid water, and not gas, was the fluid phase in the flows. We subdivide the tuff turbidite lithofacies (Table 1) into coarse-

grained tuff turbidites, massive tuff turbidites, and laminated tuff turbidites, analogous to the gravelly high-density turbidites, the sandy high-density turbidites and low-density turbidity current deposits of Lowe (1982). These are interstratified with the mudstone and siltstone lithofacies (Table 1), interpreted to record suspension and lesser dilute turbidity current sedimentation of fine-grained volcaniclastic and bioclastic detritus.

Shallow marine to littoral volcaniclastic deposits, such as beach conglomerate (Table 1), are very rare probably due to narrow paleo-shorelines along steep volcano flanks. However, bioherms may build on a variety of substrates if water temperatures are appropriate. In the Alisitos arc, shallow marine rudist reef buildup was accelerated by trapping of volcaniclastic debris between organisms. One of the distinctive features of the Alisitos arc in general is its very thick rudist reef (Table 1) bioherms of Aptain–Albian age (Allison, 1955, 1974). This carbonate debris was reworked into deep water as bioclastic turbidites with variable amounts of volcaniclastic detritus (Table 1).

3. Tectonostratigraphic and intrusive history of the Rosario segment of the Alisitos arc

Accreted oceanic arc terranes have made a sizeable contribution to the growth of continents (Busby, 2004), but these terranes are nearly always highly dismembered, making "four-dimensional" (space and time) reconstructions highly speculative. The Rosario segment of the Alisitos arc is highly unusual because it is such a large, excellently exposed, completely intact piece of an oceanic arc. This allows a time-integrated view of an oceanic arc at a level of detail that is not possible in modern examples. In this section, we use stratigraphic correlations to divide the tectonstratigraphic and magmatic history of the Rosario segment of the Alisitos arc into a series of four time slices (Fig. 7A, B, C, D). The detailed reconstructions presented in this section can be used as predictors of broadly-synchronous events in the evolution of extensional oceanic arcs. These detailed observations form the basis for new models presented in a later section. These new models for the evolution of extensional oceanic arcs could only be arrived at by using our detailed time-integrated approach in outcrop.

Through all four time slices (Fig. 7), the Rosario segment of the Alisitos arc was subaerial around its main eruptive center (Fig. 6B), and was flanked by marine basins to the present-day north (Fig. 6C) and south (Fig. 6A). The southern marine basin is interpreted as a "volcano-bounded basin" (sensu Smith and Landis, 1994), where strata accumulated in the low areas between constructive volcanic centers, in shallow water to deepwater environments (Fig. 6A). The northern marine basin, in contrast, is interpreted as a "fault-bounded basin", which was downthrown into deep water (Fig. 6C) relative to the main subaerial eruptive center along a syndepositional fault zone. This fault zone shows about 3 km of stratigraphic offset in the normal sense (Figs. 2 and 7A), crosscut by late-stage intrusions (Figs. 2 and 7D). In this section, we describe each time slice beginning with the southern, volcano-bounded basin, because that stratigraphy (Fig. 6A) is more easily related to stratigraphy on the central subaerial edifice (Fig. 6B) relative to the northern, fault-bounded basin (Fig. 6C). All map-scale lithologic units are referred to in parentheses by the map symbols for ease of comparison with the geologic maps (Figs. 2–5). The geologic maps form the basis for all of the interpretations presented in this section.

3.1. Time slice 1

The substrate for time slice 1 strata consists of extensively intruded, hornfelsed, hydrothermally altered and locally folded strata that are very difficult to analyze for protolith characteristics (e.g., see tightly folded limestone/marble on the east side of the map shown in Fig. 2). This section is dominated by silicic ignimbrites, andesitic and lesser basaltic lava flows, debris flow deposits and hypabyssal intrusions, and marine rocks appear to be absent (Fig. 2). This suggests that prior to phase 1, the Rosario segment of the Alisitos arc was well established, having already built an emergent arc platform.

The base of time slice 1 is defined by strata that can be correlated across the Rosario segment (interstratified ignimbrites and fluvial rocks, Fig. 7A) and the top of time slice 1 is defined by the base of the

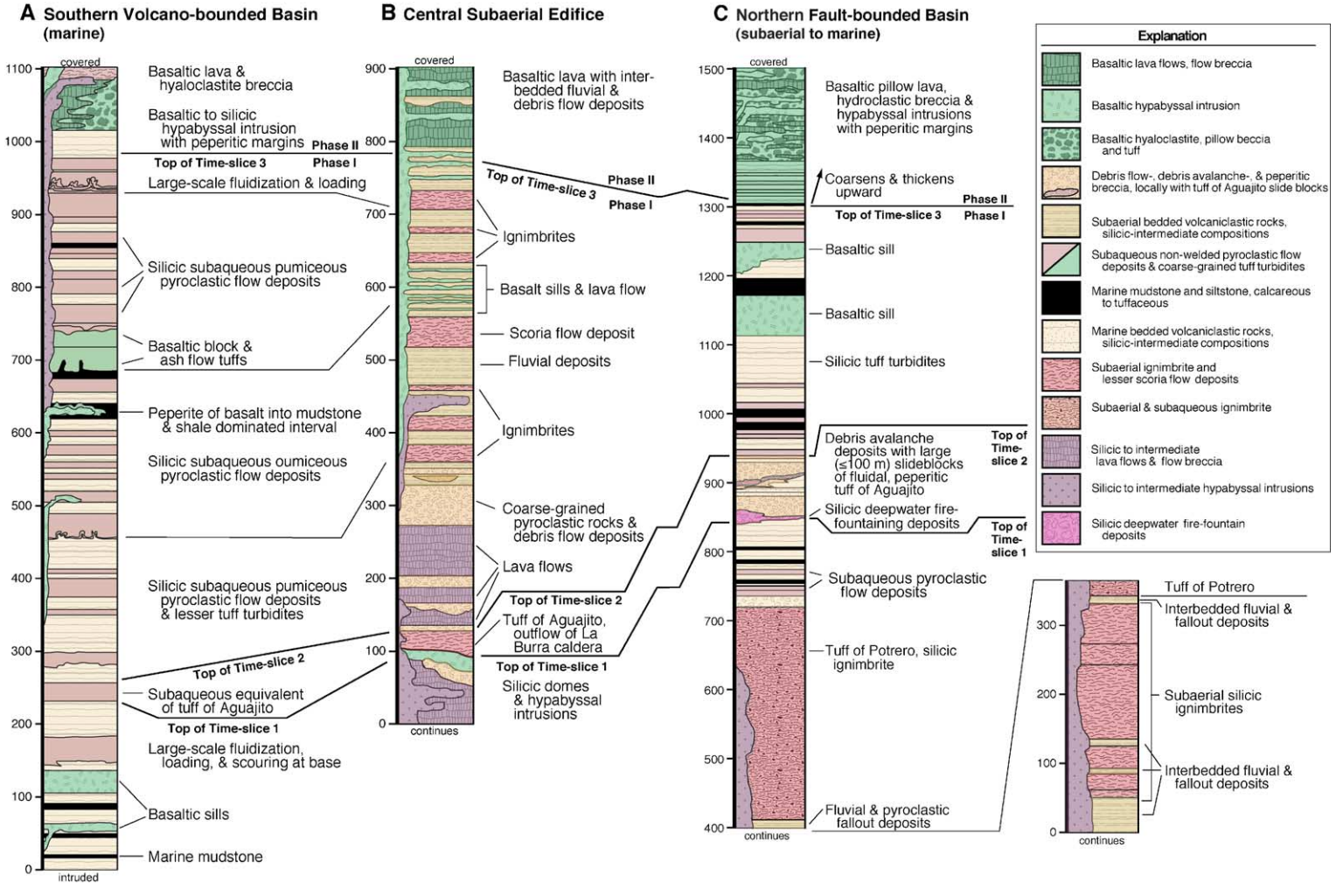

Fig. 6. Generalized measured sections from three contrasting paleo-environments, Rosario segment of the Alisitos arc.

widespread tuff of Aguajio shown on time slice 2 (Fig. 7B).

3.1.1. Southern, volcano-bounded basin

During time slice 1, the southern boundary of the southern, volcano-bounded basin was defined by an andesitic to basaltic composite cone (Fig. 7A), with lava flows, flow breccias, and hypabyssal intrusions and lesser hyaloclastite breccias and debris flow deposits (Kla, Fig. 5). Local beach conglomerates indicate that the cone was at least partly emergent.

A marine basin intervened between the andesitic to basaltic composite cone and the central emergent edifice (Fig. 7A). Sedimentary dikes and soft sediment slumps in the basin reflect volcanoseismicity during time slice 1. This basin was largely filled with mudstones, siltstones and laminated tuff turbidites (Kvm, Fig. 5) deposited in sub-wave base environments (Fig. 6A and Table 1). These alternate with mafic to intermediate hyaloclastites and pillow breccias (Kvcba, Fig. 5) presumably erupted from subaqueous vents on the andesitic to basaltic composite cone to the south. Nonwelded ignimbrites and subaqueous pyroclastic fallout (Kpf, Fig. 5) represent the marine equivalents of welded ignimbrites erupted from a leaky, incipient ring fracture on the subaerial edifice to the north (described below). Block-and-ash-flow tuffs are also present, and likely formed by lava dome collapses off the southern margin of the subaerial edifice (Kdd, Fig. 4).

3.1.2. Central, subaerial edifice

We infer that an incipient, leaky ring fracture developed on the central subearial edifice (Kvcad, Fig. 4) during time slice 1, ultimately resulting in formation of the La Burra caldera during time slice 2. This leaky ring fracture plumbed silicic pumiceous pyroclastic flows (Ki, Fig. 4) to the surface along its southern margin, and fed an andesitic center (Kha and Khla, Fig. 2) on its northern margin (Fig. 7A).

The silicic ignimbrite sheets that erupted from the southern incipient ring fracture may have extended into the area of the “proto-La Burra caldera” (Fig. 7), but this area now lies in the floor of the caldera (Ki, Fig. 2) and is too heavily altered and intruded to allow detailed protolith mapping (see stippled pattern on Fig. 7A),. The silicic ignimbrites are well preserved south of the caldera (Ki, Fig. 4), where they are ultrawelded, with flow-folded and stretched pumice, in spite of being relatively thin (2–7 m). For this reason, they are inferred to be near-vent accumulations, rather than distal equivalents of the moderately welded ignimbrites present in the northern basin (described below). The silicic ignimbrites are interstratified with dome talus breccias and lesser debris flow deposits shed from the dacite dome complex to the south (Kdd, Figs. 2, 4; domes and intrusions of Fig. 6B). The asymmetry of the deposits surrounding the dacite dome complex, i.e., block-and-ash flow tuffs to the south in the marine basin (described above), and dome talus breccias to the north on the subearial edifice, probably reflects an asymmetry in topographic gradients at the edge of the subaerial edifice, (i.e., more efficient dome collapse and disintegration of avalanche debris along the steeper slope toward the basin).

The andesitic center that was plumbed up the northern incipient ring fracture during time slice 1 is composed of andesite-clast debris flow deposits, hypabyssal intrusions, and lesser coherent lava flows(Kha and Khla, Fig. 2). This center is incompletely preserved due to later intrusion of the Los Martirez pluton (Kplm1, Fig. 2; time slice 3, Fig. 7C).

Both the ignimbrite section and the andesite center overlie a very thick section of nonmarine volcanic debris flow deposits, hyperconcentrated flood flow and dilute flow deposits, and welded ignimbrites. These are similar to strata downfaulted into the deep marine realm during time slice 1 (Kvcad, Figs. 2 and 3; Fig. 7A).

3.1.3. Northern, fault-bounded basin

The basal 3 km of fill of the northern, fault-bounded basin consists of nonmarine welded ignimbrites (Kis1 – 4 and Kis?, Fig. 3), fluvial deposits with lesser subaerial fallout tuffs and paleosols (Kff, Fig. 3) and largely nonmarine pyroclastic rocks (Kvcad, Fig. 3). These are overlain by the 400-m-thick tuff of Protrero (Kip, Fig. 3), which erupted as the basin was downdropped into deep water.

The ignimbrites below the tuff of Protrero (units Kis1-4, Fig. 3; subaerial dacite ignimbrites, Fig. 6B) are about ten times thicker than broadly coeval ignimbrites on the subaerial edifice. This may indicate that they were ponded against a basin along the fault that

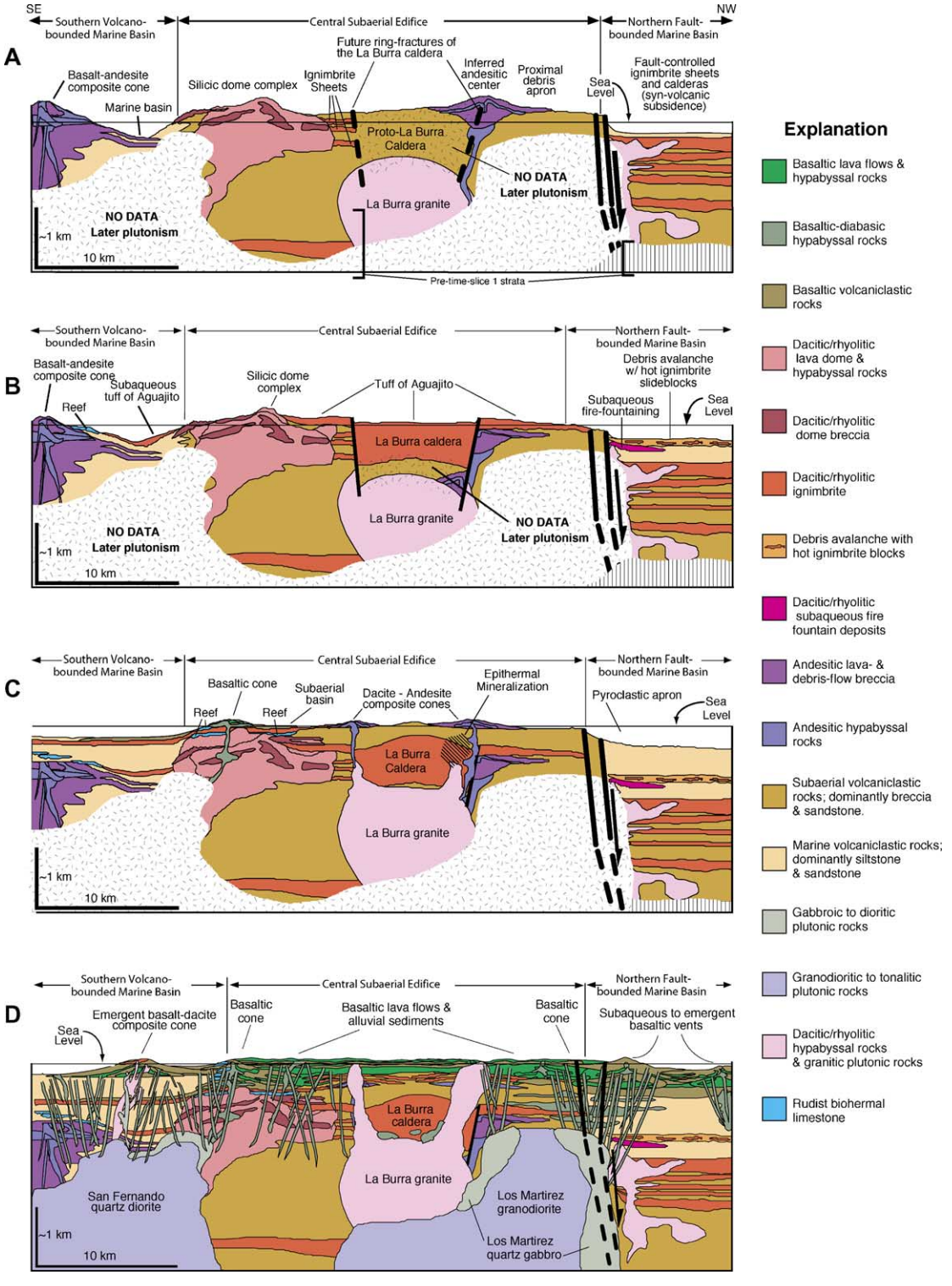
A
SE
NW
Southern Volcano-bounded Marine Basin
Central Subaerial Edifice
Northern Fault-bounded Marine Basin
Future ring-fractures of the La Burra caldera
Basalt-andesite composite cone
Silicic dome complex
Ignimbrite Sheets
Inferred andesitic center
Proximal debris apron
Sea Level
Fault-controlled ignimbrite sheets and calderas (syn-volcanic subsidence)
Marine basin
Proto-La Burra Caldera
NO DATA
Later plutonism
La Burra granite
~1 km
10 km
Pre-time-slice 1 strata
B
Southern Volcano-bounded Marine Basin
Central Subaerial Edifice
Northern Fault-bounded Marine Basin
Basalt-andesite composite cone
Subaqueous tuff of Aguajito
Reef
Silicic dome complex
Tuff of Aguajito
Debris avalanche w/ hot ignimbrite slideblocks
Subaqueous fire-fountaining
Sea Level
La Burra caldera
La Burra granite
NO DATA
Later plutonism
~1 km
10 km
C
Southern Volcano-bounded Marine Basin
Central Subaerial Edifice
Northern Fault-bounded Marine Basin
Basaltic cone
Subaerial basin
Dacite - Andesite composite cones
Epithermal Mineralization
Reef
Pyroclastic apron
Sea Level
La Burra Caldera
La Burra granite
~1 km
10 km
D
Southern Volcano-bounded Marine Basin
Central Subaerial Edifice
Northern Fault-bounded Marine Basin
Emergent basalt-dacite composite cone
Sea Level
Basaltic cone
Basaltic lava flows & alluvial sediments
Basaltic cone
Subaqueous to emergent basaltic vents
La Burra caldera
La Burra granite
San Fernando quartz diorite
Los Martirez granodiorite
Los Martirez quartz gabbro
~1 km
10 km
Explanation
Basaltic lava flows & hypabyssal rocks
Basaltic-diabasic hypabyssal rocks
Basaltic volcaniclastic rocks
Dacitic/rhyolitic lava dome & hypabyssal rocks
Dacitic/rhyolitic dome breccia
Dacitic/rhyolitic ignimbrite
Debris avalanche with hot ignimbrite blocks
Dacitic/rhyolitic subaqueous fire fountain deposits
Andesitic lava- & debris-flow breccia
Andesitic hypabyssal rocks
Subaerial volcaniclastic rocks; dominantly breccia & sandstone.
Marine volcaniclastic rocks; dominantly siltstone & sandstone
Gabbroic to dioritic plutonic rocks
Granodioritic to tonalitic plutonic rocks
Dacitic/rhyolitic hypabyssal rocks & granitic plutonic rocks
Rudist biohermal limestone

dropped the basin into deep water during the eruption of the tuff of Protrero.

The tuff of Protrero (Kip, Fig. 3) is a 400-m-thick welded ignimbrite that overlies the 3-km-thick non-marine section but passes gradationally upward into a >800-m-thick deepwater section (Fig. 6C). The tuff of Protrero is a dacite ignimbrite that can be divided into multiple flow units defined by abrupt changes in pumice sizes and concentrations. Additionally, some of the basal flow units are separated by thin beds of fluvially-reworked tuff. The top of the tuff of Portrero passes gradationally upward into a 20-m-thick debris flow deposit with volcanic rock fragments and marine fossil fragments suspended in a nonstratified matrix of fine-grained tuff. This tuffaceous debris flow deposit is identical to those within submarine calderas described by Kokelaar and Busby (1992), and are inferred to record submarine slumping of water-saturated ash off the walls of a submarine caldera during the last stages of collapse, after the eruption is finished. The tuffaceous debris flow deposits pass gradationally upward into a section of interstratified tuff turbidites, and black marine mudstones (Fig. 6C). These relations indicate that the basin subsided from a subaerial environment to sub-wave base water depths during eruption and deposition of the tuff of Protrero, requiring at least 500 m of subsidence to accommodate the accumulation of the tuff as well. This abrupt downdropping is more easily explained by caldera collapse than by tectonic subsidence. Furthermore, abundant hypabyssal intrusions with mineralogy the same as the tuff of Protrero intrude the section below the tuff (Khd, Figs. 3 and 6), suggesting that the tuff is near-vent, rather than accidentally ponded. However, caldera subsidence cannot account for continued subsidence recorded in the overlying section discussed below); therefore, we infer that the caldera was sited along a major fault zone (Fig. 7). The absence of the tuff of Protrero on the central, subaerial edifice is consistent with the interpretation that the caldera formed within a pre-existing down-faulted basin.

3.1.4. Intrusions

Plutonic equivalents to the hypabyssal intrusions and eruptive centers of time slice 1 presumably lay largely at lower structural levels that are not preserved in the accreted arc terrane (possibly due to delamination during accretion, discussed below). The possible exception to this is La Burra granite (Kplb, Fig. 2), which may have begun to form as the feeder for the incipient leaky ring fracture ignimbrite sheets (Fig. 7A).

3.2. Time slice 2

Time slice 2 is defined by strata related to the cataclysmic caldera-forming eruption on the central subaerial edifice (Figs. 2 and 7B). These strata include intracaldera and outflow ignimbrite (tuff of Aguajito, Fig. 6B) on the subaerial edifice (units Kia/Kial, Fig. 4). They also include the marine equivalent of the tuff of Aguajito in the southern, volcano-bounded basin (Figs. 6A, 8). In the northern, fault-bounded basin, the cataclysmic event is recorded by a deepwater debris avalanche deposit (Kda, Fig. 3) containing megablocks of tuff of Aguajito that were emplaced in a very hot, plastic state (Figs. 6C, 7B). Also included in time slice 2 are silicic subaqueous fire fountain deposits that underlie the debris avalanche deposit (Fig. 6C) within a section dominated by tuff turbidites and black mudstones/siltstones (Kvm, Fig. 3).

3.2.1. Southern, volcano-bounded basin

Volcanism continued from time slice 1 into time slice 2 at the basalt–andesite composite cone (Kla, Kvcba, Fig. 4), but several features suggest that it became more submerged due to a relative sea level rise (Fig. 7B). First, rudist reef deposits are intercalated with many of the hyaloclastite breccias and lava flows (see limestone marker beds in Kvcba and Kvm, Fig. 5). Second, the section contains abundant, large accretionary lapilli 4 cm in diameter, suggesting that some vents were submerged. Third, the ratio of hyaloclastite breccias (Kvcba) to coherent lava flows (Kla) is greater.

Fig. 7. Time slice reconstruction of the evolution of the Alisitos arc, Rosario segment, shown in cross-sectional view (about 60 km long). Time slices A, B, and C are interpreted to represent an extensional oceanic arc (phase 1). Time slice D is interpreted to record a rifted oceanic arc (phase 2).

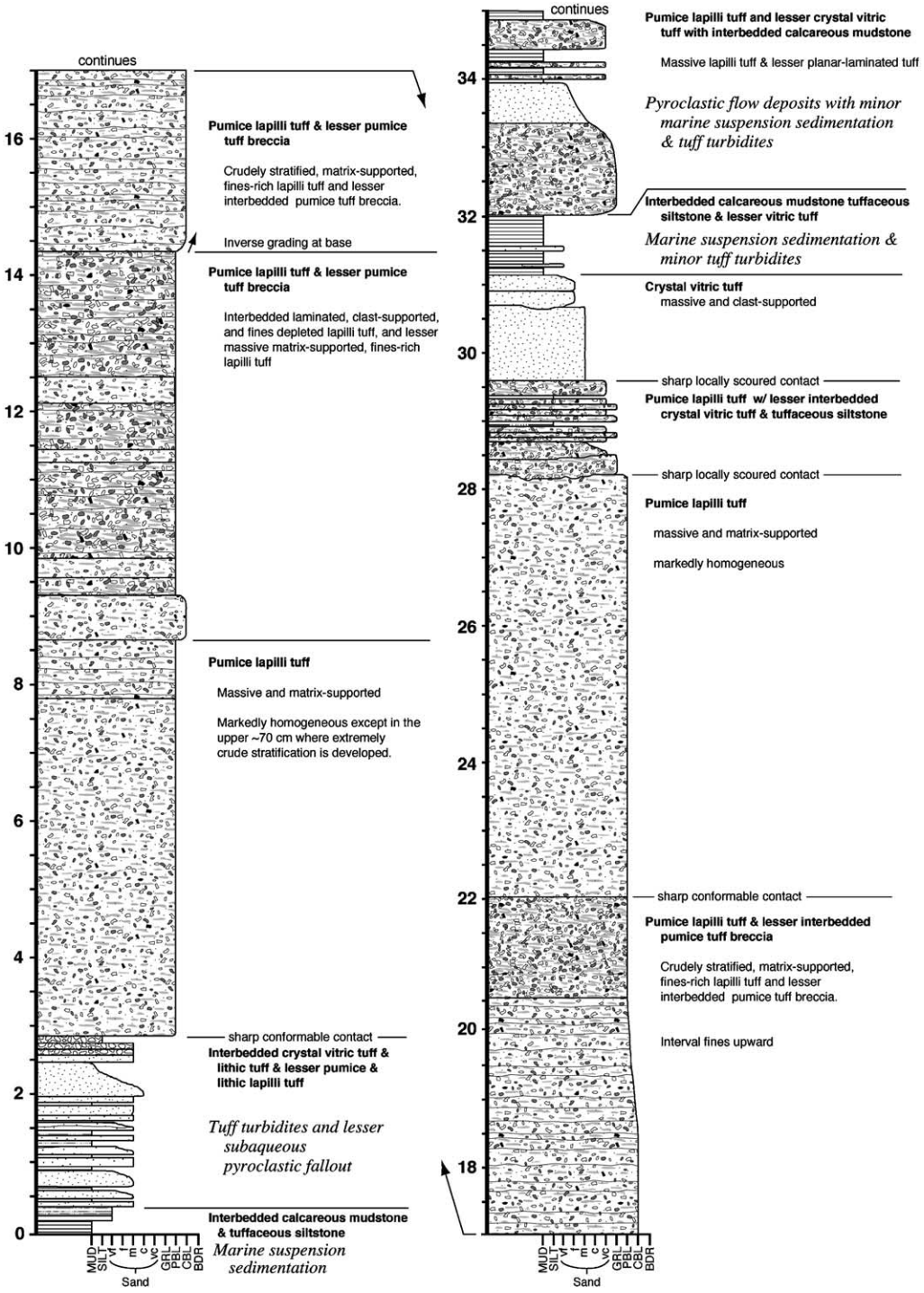

Fig. 8. Measured section of a subaqueous pyroclastic flow deposit in the southern, volcano-bounded marine basin (Fig. 5). Shown here is the subaqueous equivalent of the subaerial densely-welded to high-grade tuff of Aguajito (time slice 2, Figs. 6A, 7B).

The deepest part of the southern, volcano-bounded marine basin continued to receive "background" sediments of mud and tuffaceous silt deposited from dilute turbidity currents and suspension sedimentation below wave base (Table 1; Kvm, Fig. 5). This background sedimentation was interrupted by emplacement of the subaqueous facies of the tuff of Aguajito (Figs. 6A, 7B). On the subaerial edifice (described below), the caldera outflow facies is welded and up to 300 m thick, with vertical variability in pumice contents and sizes that hint at the presence of numerous flow units; in the more distal, subaqueous realm, the tuff is much thinner (35 m) but the distinction between flow units is much clearer (Fig. 8).

We interpret the subaqueous facies of the tuff of Aguajito as the deposits of eruption-fed pyroclastic flows that entered the marine basin largely without disintegrating at the shoreline; therefore, we include it in the ignimbrite lithofacies of Table 1. We describe its features here because they are typical of most of the other 26 subaqueously-emplaced ignimbrites in the southern volcano-bounded marine basin (silicic subaqueous pyroclastic flow deposits, Fig. 6A; pumiceous pyroclastic flow deposits (Kpf), Fig. 5). The subaqueous tuff of Aguajito consists largely of massive to crudely stratified, unsorted, ash matrix-supported pumice lapilli tuff and tuff breccia (Fig. 8). The massive intervals show possible evidence for some retention of heat upon deposition, including delicate quench fragmentation textures on some clasts (similar to those described by Cole and DeCelles, 1991; Kano et al., 1994), pervasive vesiculation of the tuff matrix, and quartzofeldspathic recrystallization. We interpret these massive intervals to represent the deposits of pyroclastic flows that experienced minimal mixing with ambient water as they entered and traversed the marine basin. The crudely stratified intervals of the subaqueous tuff of Aguajito, although dominantly unsorted, also include ash matrix-poor to clast-supported lapilli tuffs that record some elutriation though mixing of pyroclastic flows with ambient water (Fig. 8). The base and top of the subaqueous facies of the tuff of Aguajito, tuff, in contrast, have well-sorted, well-stratified crystal vitric tuffs and lesser lapilli tuffs, most in graded beds with some Bouma divisions, recording extensive mixing with water. These basal and capping tuff turbidites may have formed by disintegration of pyroclastic flows at the shoreline, or by remobilization of pyroclastic fall or flow deposits, or both.

3.2.2. Central, subaerial edifice

The La Burra caldera (Fig. 7B) is identified by a >3.2-km-thick section of welded tuff of Aguajito (base and top intruded, Ki, Fig. 2), now largely surrounded by the annular intrusion of the La Burra granite (Kplb, Fig. 2). The intrusion does not exactly correspond to the caldera boundary, however, because >2 km thickness of welded ignimbrite (base exposed, top intruded) lies north of the north ring intrusion. This >2-km-thick ignimbrite is bounded to the west by a N–S-trending fault (Fig. 2), across which the ignimbrite thins to 200 m. The fault is intruded by andesites of time slice 3 (Fig. 7C), which cut the tuff of Aguajito and predate the last phase of emplacement of La Burra granite (time slice 4, Fig. 7D, discussed below). We therefore interpret this fault to be a preserved caldera-bounding fault.

Outflow ignimbrite up to 200 m thick can be traced 2 km northward from the caldera margin before it is lost under Late Cretaceous sedimentary rocks (Ktrg, Fig. 2). The northern outflow ignimbrite appears to be missing its top, since the welded part of this sheet lies in its upper ~20 m; this may have been the source for some of the slide sheets of tuff of Aguajito within the debris avalanche deposit of the northern, fault-bounded marine basin (described below).

Tuff of Aguajito outflow ignimbrite extends 4.5 km southward from the caldera (Kia, Fig. 2), where it lenses from 300 to 0 m thickness against dome lavas and mantling breccias (Kdd, Kvcad Fig. 2) in the present-day view (Fig. 7B). Some flows must have gone around the domes, however, to feed the subaqueous facies of the tuff of Aguajito to the south in the southern marine basin (described above). The tuff is densely welded across the subaerial edifice south of the caldera area, even where it thins to only a few meters, except near the caldera margin, where it is variably welded due to the cooling effect of abundant lithic blocks, interpreted as lag breccias.

The north boundary between the subaerial edifice and the northern deepwater marine basin exposes a pair of prominent NNE-trending faults (Fig. 2) that we interpret to have been active during time slice 2 (Fig. 7B), for reasons discussed in the following section.

3.2.3. Northern, fault-bounded marine basin

In the northern fault-bounded basin, the tuff of Aguajito occurs as blocks, as much as 150 m across, that were emplaced while still very hot and plastic as part of a debris-avalanche deposit shed into deep water from the faulted basin margin, described in this section (Kda, Figs. 2, 3; Figs. 6C, 7B; Table 1). The debris avalanche deposit is directly underlain by deepwater silicic fire fountain deposits (Fig. 6C).

Deepwater silicic fire fountain deposits (Table 1) are a vent-proximal deposit up to 25 m thick that thins rapidly northward away from the south end of the basin. We infer that the deepwater silicic fire fountain deposits were erupted from a deepwater satellite vent for the tuff of Aguajita, from feeder dikes along the fault zone that formed the margin between the central subaerial edifice and the deepwater basin (Fig. 7B). We speculate that injection of feeder dikes along this fault zone triggered collapse of the north margin of the central subaerial edifice, during or very soon after the caldera-forming eruption of the tuff of Aguajito, to form the overlying debris avalanche deposit.

The deepwater debris avalanche deposit described here (Table 1) is the only example known to us of an ancient deposit exposed in outcrop, although they are very common around island volcanoes in the modern world's oceans. The deepwater debris avalanche deposit (Kda, Figs. 2 and 3) is up to 100 m thick, with blocks of tuff of Aguajito up to 150 m long and 25 m thick (Fig. 6C). It is a flat-surfaced, non-coherent debris avalanche deposit (Table 1) that extends at least 10 km from the fault-controlled paleo-coastline from which we infer it was shed, but its northern extent has not been mapped. The distal equivalent may be represented by megablock-rich debris flow deposits 30 km to the north in the San Quintín area, described below. It is largely massive, with several discontinuous stratified intervals less than a few meters thick, suggesting emplacement as multiple flow units (Fig. 6C). Noncoherent debris avalanches on land may be "dry" or they may be "wet", with water contents of >20%, resulting in a flat-surfaced deposit that transforms distally into debris flow deposits (Palmer et al., 1991; Kokelaar and Romagnoli, 1995). It seems likely that at least some of the collapses that fed the deepwater debris avalanche in the Alisitos arc consisted of shallow marine volcaniclastic sediment, because broken shells are abundant in it. Some of the flow units show graded tops, suggesting that at least some ambient water was incorporated during transport. Multiple sedimentation units within the sheet suggest emplacement in several discrete but closely-spaced events, perhaps due to retrogressive failure like that inferred for debris avalanche deposits elsewhere (Crandell et al., 1974; Voight et al., 1981; Glicken, 1986, 1991; Eppler et al., 1987; Hackett and Houghton, 1989; Siebert et al., 1995). Stratification in the Alisitos subaqueous debris avalanche deposits is accentuated relative to that described for subaerial deposits elsewhere, however, probably due to fundamentally different transport-depositional processes in the marine environment.

One of the most striking features of the Alisitos deepwater debris avalanche deposit is that its massive intervals contain very irregularly-shaped fluidal clasts of all sizes of rheomorphic (or "lava-like", ultra-welded) high-grade ignimbrite (Table 1). These centimeter- to decameter-scale clasts wrapped themselves around rigid lithic fragments, clearly retaining enough heat to remain plastic within the volcaniclastic matrix of the moving avalanche. Many of these plastically-deformed clasts show peperitic margins, where pieces of ignimbrite blocks are dispersed from the edges of blocks into the host matrix, and the matrix injects the blocks. "Peperite", defined as a mixture of magma and wet sediment, may result from quench granulation processes, steam explosions, or steam fluidization processes (e.g., Busby-Spera and White, 1987; White and Busby-Spera, 1987). Peperites commonly result from interaction between wet sediment and shallow-level intrusions, or where lava flows overlie or burrow into wet sediment. We are not aware of any study that has documented peperitic margins on an ignimbrite, much less peperitic margins on clasts of ignimbrite in an avalanche deposit, but there is no reason why "lava-like" high-grade ignimbrites could not form peperites just as lava flows do. It is clear that the clasts are of ignimbrite, and not lava, because they show the distinctive lineations present in rheomorphic tuffs, and the fabrics pass from strongly-welded to weakly-welded within individual clasts in some cases (see photos in Busby, 2004). We propose that the high-grade ignimbrite was mixed with wet volcaniclastic sediment in the rheomorphic state, producing fluidal and blocky peperite textures (defined by

Busby-Spera and White, 1987) during the avalanche process and after deposition.

The volume of the Alisitos deepwater debris avalanche is estimated at >10 km^3, assuming that its strike length is an indication of its original extent across strike. This is larger than those typically generated by sector collapse on a stratovolcano, although substantially smaller than those generated by sector collapse on a shield volcano, and is more typical of fault-controlled collapses on stratovolcanoes (Siebert et al., 1995; Ui et al., 2000). Dike injections are known to produce the largest sector collapses on Earth (Moore et al., 1994). We speculate that dike injection along the fault bound the basin to the south not only fed the satellitic fire fountain eruptions that preceded debris avalanching deposit, but also triggered the collapses that caused debris avalanching, during or very soon after eruption of the tuff of Aguajito.

3.2.4. Intrusions of time slice 2

We infer that La Burra granite is the plutonic equivalent of the tuff of Aguajita (Fig. 7B), because it is mineralogically similar to it, and because it is spatially associated with the thick intracaldera facies of the tuff. Some parts of the La Burra granite intrude the intracaldera tuff, however, in a manner typical of resurgent magmatism (Figs. 2, 4 and 7C).

3.3. Time slice 3

Time slice 3 is defined to include all of the strata above the tuff of Aguajito and the deepwater debris avalanche, and all of the strata below the widespread mafic volcanic rocks of time slice 4. Tectonic subsidence of the entire area during time slice 3 is required to accommodate the >675 m thick section in the central subaerial edifice and 800 m thick section in the southern volcano-bounded basin (Fig. 6).

3.3.1. Southern, volcano-bounded basin

Volcanism ceased at the basalt–andesite composite cone that grew during time slices 1 and 2 (eastern occurrences of Kla, Kvcba, Fig. 5) and the southern marine basin broadened during time slice 3 (Fig. 6C). The composite cone is overlain by a transgressive sequence of rudist reef and beach conglomerate, in turn overlain by laminated tuff turbidites and mudstones and siltstones and minor bioclastic turbidites (Kvm, Fig. 5), indicating local volcanic quiescence. This background sedimentation was interrupted 25 times by deposition of subaqueous pyroclastic flows that compose about 40% of the section (Kpf, Fig. 5; dacitic subaqueous pyroclastic flow deposits, Fig. 6A). These are the subaqueous equivalents of small-volume welded silicic ignimbrites erupted from ring fractures on the subaerial edifice (described below). Lesser silicic subaqueous block-and-ash flows were probably shed from the dome complex that continued to grow on the southern edge of the central subaerial edifice early in time slice 3 (Kdd, Fig. 5). These were replaced by mafic subaqueous block-and-ash flows shed from the basaltic cone that began to grow there late in time slice 3 (Klb, Figs. 5, 7C). Very limited paleocurrent data (n=5, Fackler Adams, 1997) support the interpretation that the pyroclastic flows moved southward into the basin from the subaerial edifice to the north. In contrast to strata of time slices 1 and 2 in the southern marine basin, and also in contrast to all of the marine strata in the northern fault-bounded basin, soft sediment slumps and sedimentary dikes are rare. This may indicate a reduction in relief within the southern marine basins it broadened (Fig. 7).

3.3.2. Central, subaerial edifice

The silicic dome complex at the southern edge of the subaerial edifice continued to be active from time slices 1 and 2 to the early stages of time slice 3, shedding dome breccias over the top of the tuff of Aguajito (Kdd, Fig. 4). The southern half of the silicic dome complex then became submerged, and rudist reefs were deposited on it (see lower reef deposits on Fig. 7C; also see stratigraphically lower limestone body (Klr) mapped at north end of Fig. 5, and the limestone (Klr) that overlies the dome breccia on the south end of Fig. 4). The northern reef is overlain by nonmarine rocks (Kvcad, Fig. 4) but the southern (basinward) reef is overlain by marine volcaniclastic rocks (Kvm, Fig. 5), including a subaqueous pyroclastic flow deposit (Kpf, Fig. 5). This in turn is overlain by an approximately 600-m-thick, lens-shaped body of basalt lava flows, flow breccias, hyaloclastite breccias, debris flow deposits and hypabyssal intrusions (Klb, Fig. 5; basaltic cone of Fig. 7C). A series of biohermal reefs formed on the southern edge

of this mafic cone as it grew (see limestone marker beds, Fig. 5); each bioherm is 10–30 m thick and pinches out basinward (southward) into marine volcaniclastic rocks (Kvm, Fig. 5) within a few hundred meters. This basaltic cone continued to grow during time slice 4 (Fig. 7D).

The silicic dome (early time slice 3) and the overlying basaltic cone (late time slice 3) formed the southern margin of a subaerial, probably volcano-bounded basin on the subaerial edifice. This basin filled with (Fig. 4): (1) a basal section of silicic to intermediate pyroclastic rocks (Kvcad), lava flows (Kdd) probably derived from the silicic dome to the south, and (2) an upper section of fluvially reworked andesitic to silicic tuffs (Kff), which filled from both sides with eruptive products including: (a) welded ignimbrites (Ki, Kisv) that thicken and show increased degree of welding toward the north, where we infer eruptions continued along the southern ring fracture (Fig. 7C), and (b) mafic volcaniclastic rocks (Kvcb), lava flows (Klb) and a scoria-and-ash-flow tuff (Ksc) that were probably derived from the basaltic cone to the south. Further evidence for continued eruptions along the ring fractures includes andesitic hypabyssal intrusions along the northern ring fracture (Kha, Fig. 2) that intrude strata as young as the time slice 2 tuff of Aguajito (Ki, Fig. 2) but do not intrude the entirely mafic section of time slice 4 (described below). We thus tentatively infer that silicic to intermediate eruptions occurred along both the northern and southern ring fractures of La Burra caldera during time slice 3 (Fig. 7C), but the vents for these were largely destroyed by continued intrusion of La Burra granite at the present-day level of exposure (Fig. 7D).

3.3.3. Northern, fault-bounded marine basin

Time slice 3 deposits of the northern, fault-bounded marine basin are dominated by tuff turbidites, with well-developed sorting, grading, lamination and cross-lamination (Figs. 3, 6C). This is in sharp contrast to the southern, volcano-bounded marine basin, where predominantly massive pyroclastic flow deposits dominate over tuff turbidites (Figs. 5, 6A). Over 600 m of tuff turbidite and about 75 m of subaqueous pyroclastic flow deposits accumulated in the basin during time slice 3 (Fig. 6C); we interpret these deposits to represent a pyroclastic apron that grew off the fault-bounded margin of the central subaerial edifice (Fig. 7C). Deposits on this apron record disintegration of subaerially-erupted pyroclastic flows as they moved down a very steep and irregularly faulted basin margin into deep water, becoming turbulent and incorporating water to become sorted and stratified. Very limited paleocurrent data ($n=3$) support the interpretation that the source of the tuff turbidites was the subaerial edifice to the present-day south. Mudstones and siltstones intercalated with the tuff turbidites are similar to those in the southern basin, but bioclastic turbidites are absent (Fig. 3), suggesting a rugged, faulted coastline that was too narrow to support extensive biohermal buildups.

3.3.4. Intrusions of time slice 3

In addition to the mafic hypabyssal intrusions in the basalt cone of Fig. 7C (Klb, Fig. 5) and the andesitic to silicic ring fracture intrusions (Kha, Fig. 2), described above, the La Burra granite continued to grow during time slice 3. Complex relations between granite bodies along the ring fractures include both altered and unaltered rocks cutting altered rocks, suggesting broadly synchronous intrusion and hydrothermal activity (Fig. 7C). This hydrothermal activity resulted in propylitic alteration and turquoise mineralization of the northern part of the intra-caldera tuff of Aguajito.

The basaltic cone at the southern edge of the subaerial edifice that spans time slices 3 and 4 signals the onset of the widespread mafic volcanism and diking that characterizes time slice 4. For this reason, the granodiorite, quartz diorite and gabbro intrusions (Fig. 2) shown on time slice 4 may have begun to form during time slice 3.

3.4. Time slice 4

The base of time slice 4 is defined as the onset of widespread mafic volcanism, sedimentation, and intrusive activity, including abundant dikes (Fig. 7C). We interpret the widespread mafic magmatism to record arc rifting.

3.4.1. Southern, volcano-bounded basin

During time slice 4, a composite cone filled much of the southern marine basin as it grew from submarine to partly subaerial environments and evolved from

mafic to intermediate to silicic compositions (Fig. 5). Mafic intrusions formed peperitic breccias within turbidite host sediments beneath the composite cone (Fig. 6A), and mafic hyaloclastite breccias, fire fountain deposits and flows were erupted at the surface (unit Kvcba, Fig. 5). These vent facies deposits pass laterally into mafic pillow breccias, debris flow and tuff turbidites (also included in unit Kvcba, Fig. 5). The mafic section contains an up to 200-m-thick andesite lava (unit Kla, Fig. 5). These strata are in turn overlain by the tuff of San Fernando, a >100-m-thick silicic tuff (unit Kisf, Fig. 5) that is densely welded, presumably recording emergence of the composite cone; this lies at the top of the exposed section (Fig. 6A). The entire section is intruded by dacitic dikes and stocks (Khd, Fig. 5).

Despite the growth of the composite cone in the southern marine basin, a narrow marine basin persisted between it and the basaltic cone that continued to grow on the southern edge of the subaerial edifice during time slices 3 and 4 (map unit Klb, Fig. 5). This is recorded by the rudist reef limestone that lies near the top of the section (Fig. 5), as well as by tuff turbidites and pillow breccias shed from the southern composite cone northward into the narrow marine basin (map unit Kvcba, Fig. 5).

3.4.2. Central, subaerial edifice

By time slice 4, the central subaerial edifice was transformed from a subaerial stratovolcano with a summit caldera, to a flat, low-lying platform or basin that accumulated mafic lava flows and nonmarine mafic fragmental rocks (Fig. 7D). The mafic lava flows and lesser scoria flows form laterally continuous sheets of even thickness, indicating a lack of relief (Klb, Figs. 2, 4); Ksc, Fig. 4). Abundant interstratified alluvial deposits (Kvcb, Fig. 4) are composed entirely of mafic clasts that could have been derived at least in part from the basaltic cone that continued to grow on the south edge of the platform. Rudist reefs on the south flank of the basaltic cone, described above, show that the subaerial platform lay near sea level. We speculate that basaltic cones fringed the subaerial platform (Fig. 7D), producing a volcano-bounded basin that accumulated mafic fragmental rocks, but the north edge of the platform is covered by younger sedimentary rocks, so we cannot prove this.

As discussed below, recent studies of modern rifted arcs show that they subside rapidly below sea level. This submergence is not recorded in time slice 4 strata of the Rosario segment, because the record is incomplete; only a ≈200m thick section is exposed on the central subaerial edifice, with the top unconformably overlain by sedimentary rocks. In the San Quintín segment to the north, however, submergence of the entire arc platform is recorded by deposition of apparently widespread sandstone turbidites (Fig. 10).

3.4.3. Northern, fault-bounded marine basin

The onset of mafic volcanism is most abrupt in the northern, fault-bounded marine basin, where no mafic volcanic rocks occur in 1–3, and time slice 4 is composed entirely of mafic volcanic and volcaniclastic rocks (Ksh, Kvcb, Klb, Fig. 3). In this basin the switch to basaltic volcanism is recorded by an upward-coarsening sequence of mafic tuffs and lapilli tuffs (Fig. 6C) deposited from turbidity currents and suspension fallout (map unit Ksh, Fig. 3). This passes upward (Fig. 6C) into coarse-grained mafic volcaniclastic deposits, including hyaloclastite breccia, pillow breccia, coarse-grained tuff turbidites and spatter deposits (map unit Kvcb, Fig. 3), with interstratified lava flows and sills (map unit Klb, Fig. 3). Diabasic to gabbroic dikes, sills and laccolithic bodies up to 4 km long are abundant within time slice 4 strata, and also intrude the top of time slice 3 strata (map unit Khb, Fig. 3). The sills and laccoliths exhibit both sharp and peperitic contacts with their hosts. In summary, the early time slice 4 basin fill records extrabasinal mafic volcanism in an adjacent area, possibly on the central subaerial edifice, but most of the section records intrabasinal mafic volcanism at subaqueous centers, although some deposits (e.g., coherent lava flows and spatter deposits) could have accumulated on emergent areas (Fig. 7D).

3.4.4. Intrusions of time slice 4

Mafic dikes cut vertically through strata of all 4 time slices (Figs. 3, 5), showing sharp contacts with 1–3 strata, and in places forming peperitic contacts with time slice 4 strata. They are thus inferred to be feeders for the basalt volcanic–volcaniclastic rocks and peperitic sills of time slice 4. The dikes show a strong alignment in a present-day NE–SW direction,

parallel to the faults that lie between the central subaerial edifice and the northern fault-bounded deep marine basin (Fig. 9). Mafic dikes are notably absent from La Burra granite, La Burra caldera and overlying strata (Figs. 4, 7D). This suggests that extension in this area was accommodated by ongoing movements in a still ductile La Burra granite, and that the granite was still molten enough to occlude the basalts. A similar lack of faults (and presumably, at depth, dikes) has been noted in the immediate vicinity of young calderas in the Izu–Bonin arc (Taylor et al., 1991; Taylor, 1992; Murakami, 1996).

All of the plutons in the Rosario segment appear to have been active during time slice 4. Ongoing intrusion of La Burra granite is indicated by the fact that it cross-cuts strata of time slices 3 and 4 (Kplb, Figs. 2, 4). To the north of that, Los Martirez pluton has a gabbroic rim (Kplm2, Fig. 2) that may represent a source for some of the time slice 4 mafic dikes and volcanic rocks (Fig. 7D). The granodioritic phase of Los Martirez pluton is inferred to be younger than the gabbro and the granite, because it cuts upsection across both to intrude 1–4 strata (Kplm1, Figs. 2 and 3). Furthermore, it postdates all movement on the NNE-trending fault zone that separates time slices 1 and 2 strata of the subaerial edifice to the south from time slice 4 marine basin fill to the north (Fig. 2). Like the Los Martirez pluton, the San Fernando pluton (Kpsf) has a gabbroic rim that may similarly represent an early phase to the dominantly dioritic–tonalitic pluton (Fig. 1).

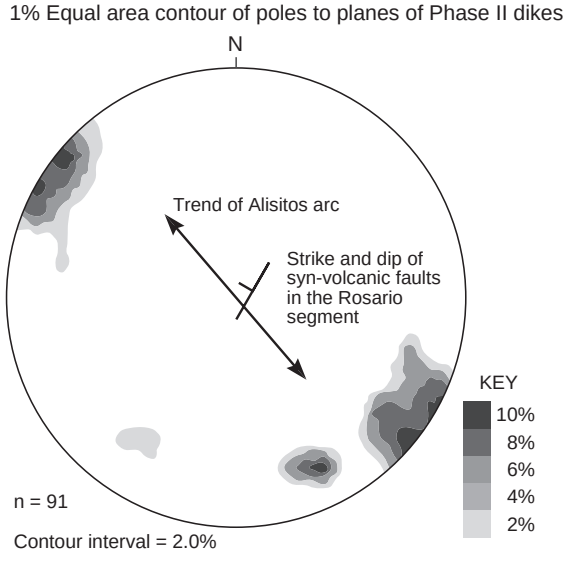

Fig. 9. Orientations of mafic dikes emplaced during time slice 4 (Figs. 3, 5) in a rifted oceanic arc setting (Fig. 7D), Rosario segment of the Alisitos arc (Fig. 2).

4. Tentative regional correlations: San Quintín segment of the Alisitos arc

We have shown that the effects of the climactic caldera-forming eruption of the tuff of Aguajito can be traced across the 50-km-long Rosario segment of the Alisitos arc (Figs. 2, 6 and 7B), in the form of very densely welded tuff on the central subaerial edifice (Fig. 4), unwelded pyroclastic flow deposits in the southern, volcano-bounded marine basin (Fig. 6), and debris avalanche deposits with fluidal ignimbrite megablocks in the northern, fault-bounded marine basin. In this section, we make tentative correlations to the San Quintín segment (Fig. 1) and propose that the effects of this eruption were recorded across a 100-km-long segment of the Alisitos arc.

The two longest and deepest canyons in the San Quintín segment that expose stratigraphy (and not mainly intrusions) are Canon El Quiote and Canon San Simon. Both canyons trend approximately ENE–WSW across the strike of bedding, which is NW–SE and dips west, similar to the Rosario segment, except that dips are gentler (about 10°) than they generally are in the Rosario segment (mostly 20–30°). Strata appear unfaulted except for one NE–SW-trending fault with less than 100 m of displacement in Canon San Simon.

We tentatively correlate a 60-m-thick welded ignimbrite in the Canon El Quiote section (Fig. 10) with the tuff of Aguajito. The welded ignimbrite, however, closely resembles the tuff of Aguajito in several ways: both tuffs are thicker and are more densely welded than any other ignimbrites, both lack lithic fragments entirely, and they have the same mineralogy, with 2% quartz and 15% plagioclase.

We also tentatively correlate a 60-m megablock-bearing debris flow deposit in the Canon San Simon section (Fig. 10) with the debris avalanche deposit in the Rosario segment. The megablock-bearing debris avalanche deposit is distinctive for its abundant cob-

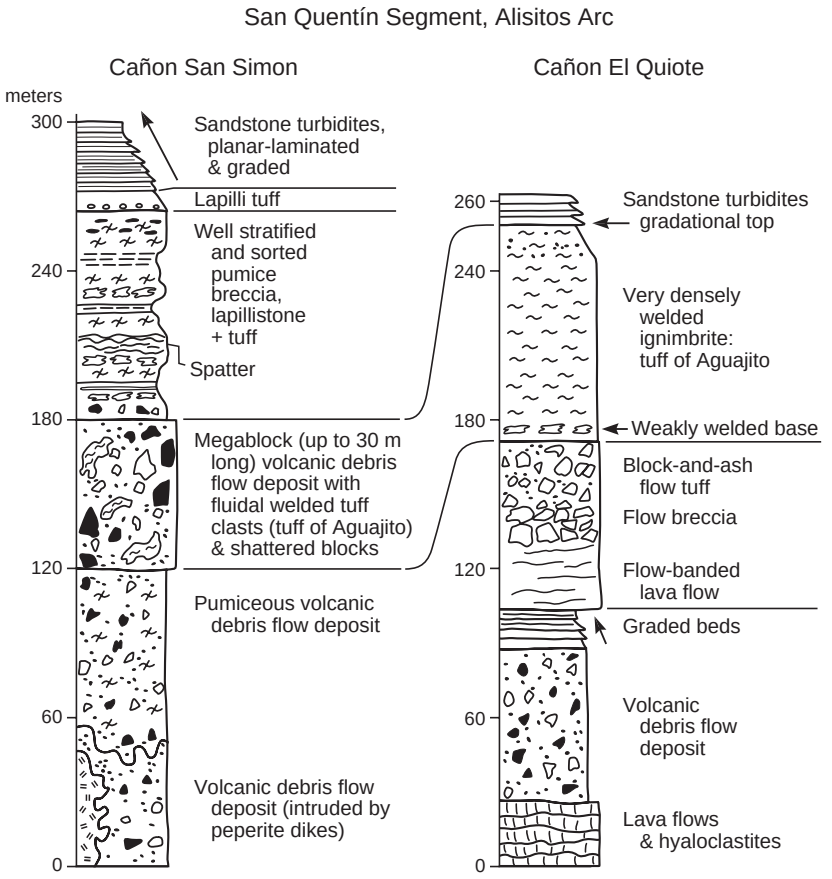

Fig. 10. Generalized measured sections from two major canyons in the San Quintín segment of the Alisitos arc (locality on Fig. 1).

ble-to boulder-sized clasts of very densely-welded tuff with the characteristics of the tuff of Aguajita (described above). It is also distinctive for its very large volcanic blocks, up to 30 m in length. The 60-m-thick pumiceous debris flow deposit that underlies the mega-block bearing debris flow (Fig. 10) is unusual for its abundance of pumice, suggesting that it too may have a genetic relationship with the climactic caldera-forming eruption and ensuing edifice collapse in the Rosario segment.

5. U–Pb zircon age controls

Rudist reef deposits do not provide very good age constraints on the age of the of the Alisitos arc, since "Aptian–Albian" (Allison, 1974) spans perhaps 25 MY. The rocks are probably too altered for Ar/Ar dating to be effective, so we sampled several volcanic units and two of the plutons to date by the U–Pb zircon method.

The plutonic rocks (Fig. 11A, B) yielded abundant zircon, and yielded excellent age results. These zircon samples were analyzed using the new "chemical abrasion" methods of Mattinson (e.g., 2003, 2005). Prior to partial dissolution analysis the zircons were subjected to high-temperature annealing. This eliminates virtually all of the radiation damage-related leaching effects that occur in some multi-step dissolution analyses (e.g., Mattinson, 1997). The zircons were then digested in a series of partial dissolution steps at progressively increasing temperatures. In both cases, the initial 1–2 dissolution steps successfully removed parts of the zircon grains that had experienced Pb loss. The remaining steps gave a series of $^{206}Pb^*/^{238}U$ ages that define a plateau. For each of the plateau steps, the

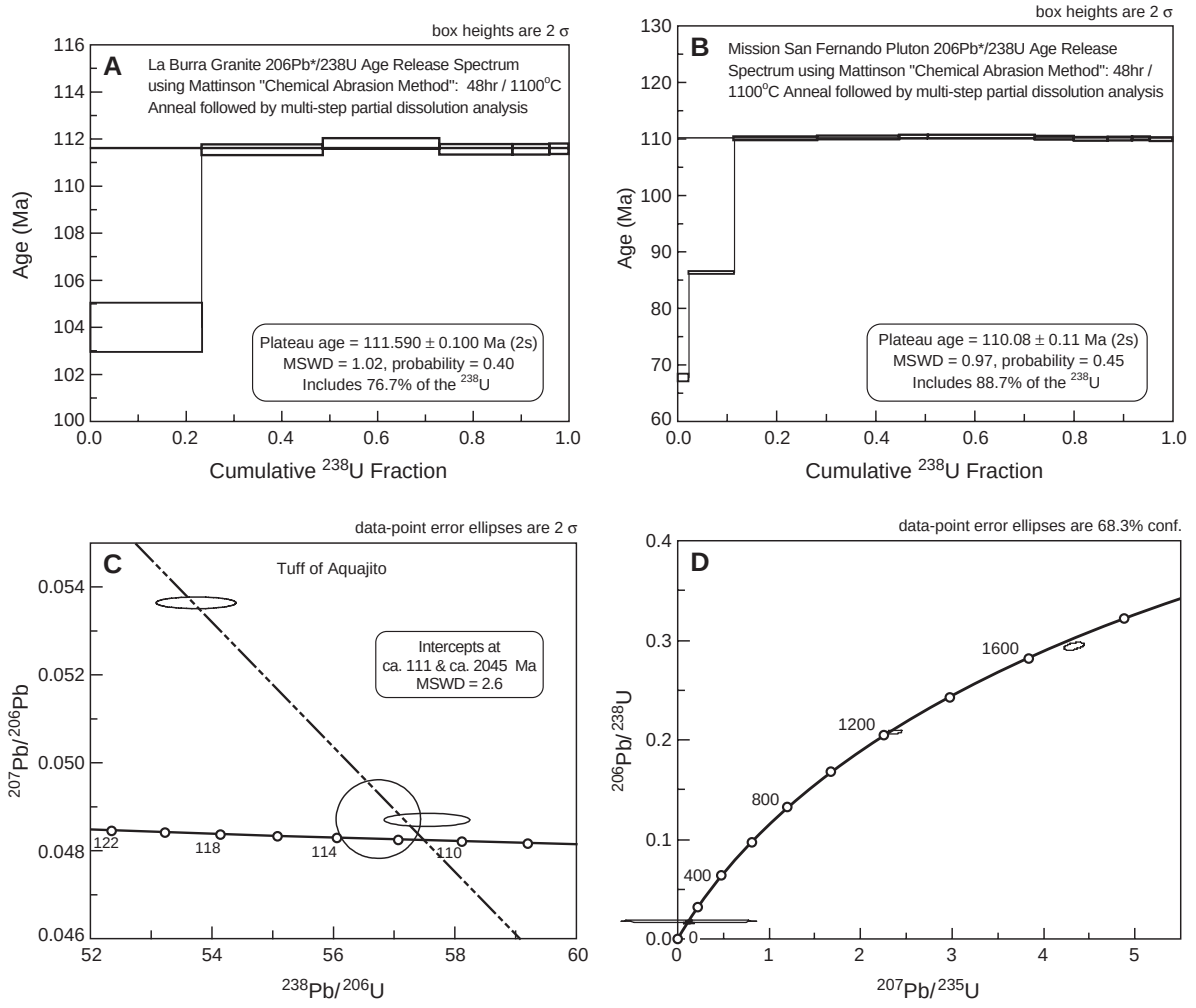

Fig. 11. U–Pb zircon ages. Concordia plots for multigrain mass spectrometer isotope dilution analyses of samples from the Rosario segment of the Alisitos arc, including (A) La Burra granite, (B) Mission San Fernando pluton, and (C) tuff of Aguajita (data in Table 2). (D) Concordia plot for single grain ICPMS analysis of tuff of Aguajito ample from the San Quentin segment of the Alisitos arc: 3 Cretaceous magmatic zircons and two Proterozoic detrital zircons (data in Table 3).

measured $^{207}Pb^*/^{206}Pb^*$ age is consistent with concordance within decay constant errors, intermediate daughter product corrections, etc. Overall, the data are consistent with complete elimination of Pb loss effects, and of a lack of any significant older inherited zircon components. Thus we have a high level of confidence that the $^{206}Pb^*/^{238}U$ plateau ages represent the magmatic crystallization ages of these plutons. The pluton of Mission San Fernando (Kpsf, time slices 3 to 4, Figs. 2, 5, 7) yields a $^{206}Pb^*/^{238}U$ plateau age of 110.08 ± 0.11 Ma (Fig. 11B, Table 2). The La Burra granite (2–4) yields a $^{206}Pb^*/^{238}U$ plateau age of 111.59 ± 0.10 Ma (Fig. 11A, Table 2).

The volcanic rocks presented greater challenges. We targeted quartz-phyric ignimbrites but, as is typical of oceanic arc volcanic rocks, the zircon yields were very low, commonly less than 1 mg from a 40-kg sample, and some samples yielded no zircon at all. Most of the volcanic zircons were high in uranium, which causes heavy radiation damage and increases the potential for Pb loss. In addition, some samples showed evidence of inheritance. The volcanic samples were analyzed at an

Table 2
Zircon data

Sample	Step	Time/temp	% tot U	$^{206}Pb/^{204}Pb$	$^{206}Pb^*/^{238}U$	6/8 Ma	$^{207}Pb^*/^{206}Pb^*$	7/6 Ma (±)
MSF Pluton	A	24 h/120 °C	1.66	23.7	0.010566	67.75	na	na
	B	24 h/160 °C	9.19	48.9	0.013489	86.38	na	na
	C	24 h/170 °C	12.33	440	0.017214	110.02	0.049825	184 (30)
	D	24 h/180 °C	16.31	5680	0.017238	110.18	0.048331	113.4 (4)
	E	24 h/180 °C	10.08	13,508	0.017259	110.31	0.048357	114.8 (2)
	F	24 h/190 °C	19.01	19,962	0.017263	110.33	0.048331	113.4 (1.5)
	G	24 h/190 °C	11.03	26,600	0.017228	110.12	0.048325	113.2 (1)
	H	24 h/190 °C	9.78	31,500	0.017198	109.92	0.048304	112.1 (1)
	I	24 h/190 °C	3.37	40,200	0.017206	109.98	0.048311	112.4 (1)
	J	24 h/190 °C	4.31	35,500	0.017211	110.00	0.048299	111.9 (1)
	K	72 h/240 °C	2.91	4430	0.017191	109.88	0.048315	112.7 (1)
		total U (ppm)	391.7					
La Burra Pluton	A	12 h/140 °C	23.34	180.3	0.016264	104.00	0.048959	144 (65)
	B	12 h/150 °C	25.33	9950	0.017449	111.52	0.048352	114.6 (2)
	C	12 h/160 °C	24.35	71,100	0.017492	111.79	0.048392	116.6 (1)
	D	12 h/160 °C	15.23	80,900	0.017452	111.54	0.048389	116.4 (1)
	E	12 hr/160 °C	7.72	65,100	0.017453	111.54	0.048392	116.6 (1)
	F	12 h/160 °C	4.02	52,100	0.017457	111.56	0.048407	117.6 (1)
		total U (ppm)	1,306					
Potrero tuff	1B	72 h/240 °C	9.13	1801	0.017017	108.8	0.048287	109 (10)
	2B	72 h/240 °C	na	2159	0.017457	111.6	0.048617	127 (16)
Aguajito tuff	1C	72 h/240 °C	0.42	5705	0.017379	111.1	0.048696	131 (6)
	2C	72 h/240 °C	0.30	657	0.017623	112.6	0.048723	135 (35)
	3C	72 h/240 °C	2.77	4851	0.018608	118.9	0.053638	354 (4)
San Vinc. tuff	1B	72 h/240 °C	23.27	26,210	0.016512	105.6	0.048379	116.1 (1)
	2B	72 h/240 °C	na	1531	0.016927	108.2	0.048377	115.8 (8)
	3B	72 h/240 °C	15.39	9799	0.017175	109.8	0.048359	115.0 (3)
C San F Ignim	1B	72 h/240 °C	6.36	3196	0.017291	110.5	0.048415	117.7 (7)
	2B	72 h/240 °C	3.03	2539	0.017322	110.7	0.048475	120.6 (7)

1)"Step" refers to individual partial dissolution steps. For the plutonics, all steps are shown; for the volcanics, only the final step.
2)"Time/temp" gives conditions for each partial dissolution step. All used 50% HF.
3)"% tot U" is the % of the total U in the zircon fraction released by each step.
4)"7/6 Ma" is the calculated $^{207}Pb^*/^{206}Pb$ age, corrected for 80% exclusion of ^{230}Th during magmatic crystallization. This reduces the "raw" 7/6 age by ca. 1.9 Ma in this age range.

early stage of the study, prior to the development of the "chemical abrasion" method. Instead, the zircons were analyzed using a "simple" multi-step dissolution technique (Mattinson, 1994). Because of the high uranium concentrations (causing high levels of radiation damage), most of the zircon dissolved in one or two early, low-intensity steps. As a result, the residues were very small, some residual Pb loss effects might have persisted, and/or the residue results might reflect some minor leaching effects from the earlier partial digestion steps. Nevertheless, the results from the volcanic zircon residues are completely consistent with the ages determined from the plutonic rocks discussed above.

Two fractions of zircon (A and B) of the tuff of Potrero (time slice 1) yield $^{206}Pb^*/^{238}U$ ages of 108.8 and 111.6 Ma, respectively. The $^{207}Pb^*/^{206}Pb^*$ ages are concordant to barely concordant with the $^{206}Pb^*/^{238}U$ ages within errors, but the difference in the $^{206}Pb^*/^{238}U$ ages for the two fractions suggests slight Pb loss effects persist in the A fraction. The age of the B fraction is more likely a better measure of the eruption age of this tuff, but we cannot completely rule out very slight inheritance, due to the relatively large uncertainty in the $^{207}Pb^*/^{206}Pb^*$ age.

Zircons from the tuff of Aguajito (time slice 2) show clear evidence of inheritance of Proterozoic zircons. Three fractions yield a lower intercept age of ca 111 Ma, (Fig. 11C). Owing to the large errors and limited spread of these data points, this intercept age is only crudely determined and does not refine the

age of the section. Nevertheless, the intercept age is consistent with the ages of the contemporaneous plutons. The upper intercept age is even more poorly determined at ca 2000 Ma, but this clearly shows that some of the volcanics of the oceanic arc terrane display inheritance, consistent with the interpretation that the arc fringed a continent (Busby, 2004).

Three fractions of zircon from the tuff of San Vincente ignimbrite (time slice 3) yield $^{206}Pb^*/^{238}U$ ages ranging from 105.6 to 109.8 Ma, despite having similar $^{207}Pb^*/^{206}Pb^*$ ages. This suggests a range of minor Pb loss in these fractions, with the oldest age of 109.8 Ma approaching the original crystallization age most closely. Again, these data do not refine the age range of the section, but they are consistent with the well-determined ages of the plutons.

Two fractions of zircon from the ignimbrite at the top of the San Fernando section (time slice 4) yield identical $^{206}Pb^*/^{238}U$ ages of ca 110.6 Ma. The $^{207}Pb^*/^{206}Pb$ ages are nominally slightly older, but actually just overlap within analytical errors and decay constant errors. Thus the data could be considered concordant within errors. However, the data cannot rule out a very small amount of inheritance of older zircons. In the former case, assuming removal of all Pb loss effects, the age of 110.6 Ma would represent the crystallization age of the ignimbrite. In the latter case, again assuming removal of all Pb loss effects, the $^{206}Pb^*/^{238}U$ age would be very slightly older than the crystallization age. In either case, the consistency with the high quality pluton ages is excellent.

For purposes of correlation, we sampled the ignimbrite in the San Quentin segment that we correlated with the tuff of Aguajito on lithologic grounds (Fig. 10). Again this yielded very few zircons, and we hand-picked several grains for analysis, including rounded zircon grains in hopes of determining the provenance of inherited grains. These single crystal analyses were done by George Gehrels at the University of Arizona, using the ICP-MS techniques (see data repository item 2). The results are plotted on Fig. 11D (Pb/U concordia diagram of Ludwig, 2001; data in Table 3). Five analyses cluster with $^{206}Pb^*/^{238}U$ ages between 100 and 115 Ma, whereas two grains yield $^{206}Pb/^{207}Pb$ ages of ~1748 and ~1259 Ma. The young grains presumably record the age of magmatism within the arc, based on their consistency with the higher precision TIMS ages discussed earlier. The Proterozoic grains clearly originated in older continental crust. Southwestern North America is a likely source for grains of these ages, based on the widespread occurrence of igneous rocks (Hoffman, 1989) and detrital zircons (Stewart et al., 2001) of appropriate age in the region. This is consistent with the interpretation that the arc fringed North America (Busby, 2004) rather than representing an exotic arc accreted through closure of a major ocean basin (Dickinson and Lawton, 2001); however, more zircon samples are needed to prove this.

In summary, all of the events shown in Fig. 7 probably took place in about 1.5 MY. Our data show that the specific sample we analyzed from the La Burra

Table 3
U–Pb isotopic data from ICPMS analyses

U (ppm)	$^{206}Pb/^{204}Pb$	U/Th	$^{206}Pb/^{238}U$ ratio	± (%)	$^{207}Pb/^{235}U$ ratio	± (%)	Error corr.	$^{206}Pb/^{238}U$ age (Ma)	± (Ma)	$^{207}Pb/^{235}Pb$ age (Ma)	± (Ma)	$^{206}Pb/^{207}Pb$ age (Ma)	± (Ma)
6901-F													
51	3411	5	0.11719	2.08	0.01581	12.12	0.17	101	2	113	14	360	135
7	2580	6	0.11919	4.71	0.01778	411.62	0.01	114	5	114	405	130	4841
13	26587	4	4.33414	0.087	0.29390	1.65	0.52	1661	16	1700	70	1748	13
16	3168	10	0.12705	2.91	0.01769	16.52	0.18	113	3	121	21	290	186
13	51953	3	2.36423	0.69	0.20765	2.37	0.29	1216	9	1232	55	1259	22
30	3107	5	0.09747	1.45	0.01581	24.70	0.06	101	2	94	24	−71	301
31	15544	4	0.11885	2.09	0.01598	32.94	0.06	102	2	114	39	369	370

U concentration and U/Th have uncertainty of ~25%. $^{206}Pb/^{238}U$ and $^{206}Pb/^{207}Pb$ ratios have been corrected for fractionation by comparison with a zircon crystal with known age of 564 ± 4 Ma by TIMS (G. Gehrels, unpublished data). Uncertainties are shown at 1-sigma level, and include only measurement errors. Common Pb correction is from measured $^{206}Pb/^{204}Pb$, with composition from Stacey and Kramers (1975) and uncertainties of 1.0 for $^{206}Pb/^{204}Pb$ and 0.3 for $^{207}Pb/^{204}Pb$.

granite is 1.5 Ma older than the specific sample we analyzed from Mission San Fernando pluton. However, detailed geochronological studies of plutons elsewhere in the world show that a single pluton may be emplaced in stages that cover at least that much time, so we do not attach any geologic significance to the difference in ages between the two pluton samples. In fact, we infer that at least some phases of the La Burra granite were active in all four time slices shown on Fig. 7.

6. Time-integrated view of an intact oceanic arc: discussion

Our views of active island arcs represent only partial snapshot images, since most or all of the rocks are hidden under water and deeply buried (Clift and Lee, 1998). Nor can one use along-strike changes in an unzipping arc to construct a model for evolutionary stages in arc rifting because of along-strike variability in factors such as mantle wedge characteristics, the volume and composition of subducting sediment, and so on (Arculus et al., 1995; Clift and Lee, 1998). Drill cores through relatively distal ash deposits provide the longest temporal record possible in an active arc setting, but these sites receive ash fallout from a great number of volcanoes; cores through proximal deposits give a more coherent view of evolutionary stages in rifting, but sedimentation rates are so high, that little time is represented by them (Clift and Lee, 1998). Outcrop studies of uplifted oceanic arc terranes provide a detailed three-dimensional view, but most become dismembered and metamorphosed in the accretion process, and many are poorly dated or poorly exposed. Other arc terranes have been studied in detail (e.g., Koheena, Talkeetna and Connemara; Clift et al., 2002, 2003, 2004; Draut and Clift, 2001, Draut et al., 2002, 2004). The Rosario segment of the Alisitos arc, however, is unusual for its excellent preservation. Our time-integrated view of an intact oceanic arc terrane allows us to make predictions that may be borne out by future work in modern oceanic arcs.

The scales of the features described in this paper are the same as those present in modern oceanic arcs. For example, the diameter of the summit caldera on Raoul Island is about 7 km, and the basal dimensions of the volcanic island are about 20×30 km (Worthington et al., 1999); these are similar to the widths of the central subaerial edifice and caldera described here. Subsidiary cones and domes on surface of Raoul are 0.5–5 km wide and 100–250 m high, and some are polygenetic (Worthington et al., 1999), similar to the cones and domes described here (Fig. 7). The chief advantage of our outcrop study is that we can describe these features in detail, through space and time.

The time-integrated view presented here is highly dependent on dividing the history of the oceanic arc into time slices, through detailed geologic mapping. However, volcanic lithofacies are notoriously lenticular, with rapid lateral variations, and facies models are not as well developed as they are for sedimentary (silicilastic) systems tracts. In this study, the time-integrated view was constructed using the following:

(1) The widespread nature of ignimbrites (see Busby et al., 2005). Also in this study we correlated strata that contain distinctive clasts of rheomorphic ignimbrite, emplaced within avalanche deposits while still very hot.
(2) Recognition of mappable lithofacies associations. Most of the map units (Figs. 2–5) include two or more of the lithofacies "building blocks" presented in Table 1, and some include as many as eight. Sedimentologists have long recognized the correlation value of mapping cogenetic tracts of facies (Galloway, 1989). We use a similar approach with volcanic facies; for example, one "cogenetic tract of lithofacies", or mappable body, would be coherent lavas mantled by lava dome breccias, passing outward into a apron of block-and-ash-flow tuffs, in turn fringed by debris flow deposits of similar dominant composition.
(3) Recognition of time-transgressive processes through detailed mapping of interfingering or intrusive relationships. These are the complex map patterns between deposits that record essentially instantaneous events (such as emplacement of an ignimbrite, or growth of a single rudist patch reef), and deposits that result from protracted or repeated events, such as the growth of a basalt–andesite composite cone (Fig. 7A, B), a silicic dome complex (Fig. 7A,

B), a basaltic cone (Fig. 7C, D), or a granitic body (Fig. 7A, B, C, D).

Unconformity surfaces are commonly used as boundaries to divide stratigraphic successions into broadly-correlative sequences (van Wagoner et al., 1988). This technique has been very widely applied to sedimentary successions, and we have begun to use it in volcanic successions, particularly in subaerial continental arc paleo-environments, where erosional surfaces are commonly very deep (DeOreo et al., 2003; Busby et al., 2003; Bassett and Busby, 2005). However, there is a very notable lack of erosional unconformity surfaces in the Alisitos arc, even on the subaerial edifice, despite the fact that the nonmarine deposits are dominated by friable, easily eroded volcaniclastic material.

In continental arcs, a lack of erosional unconformities is an indicator of very high tectonic subsidence rates due to rapid extension (Cole, 1984; Busby-Spera, 1988; Smith and Landis, 1994; Busby et al., 2005). Extensional continental arc successions also have a dearth of epiclastic detritus, not only because the volcanic centers are buried (not eroded), but also because extensional arcs have the highest magma output rates on Earth, largely as pyroclastic ejecta, which buries fault scarps (Busby et al., 2005). Far less is known, however, about unconformities and the composition of detritus in extensional oceanic arcs. On the basis of our work in the Alisitos arc, we predict that drill cores through modern extensional oceanic arc platforms would encounter few epiclastic deposits and no evidence for significant erosional unconformities. Indeed, a lack of major unconformities is well documented by seismic and ODP core data through the proximal forearc region of the extensional Tonga arc (Tagudin and Scholl, 1994; Tappin, 1994).

Our maps (Figs. 2–5) document a high proportion of silicic volcanic rocks (i.e., bearing euhedral quartz phenocrysts, Table 1). Silicic volcanic rocks (with >63% SiO2) are a minor component of most oceanic arcs. As more exploration of the sea floor takes place, however, it becomes increasingly clear that many modern oceanic arc volcanoes have silicic calderas at their summits (Lloyd and Nathan, 1981; Kasuga and Kato, 1992; Monzier et al., 1994; Fiske et al., 1995; Naka et al., 1995; Lloyd et al., 1996; Wright et al., 1998; Wright and Gamble, 1999; Worthington et al., 1999; Izasa et al., 1999; Glasby et al., 2000). The newly-discovered modern examples of oceanic arc calderas provide "snapshots" of the present day, while the ancient Alisitos arc example provides evidence that many more horizons of silicic volcanic rock lie buried beneath those at the surface. All of these calderas have formed in areas of regional or localized extension.

Voluminous felsic volcanism has been attributed to regional-scale, active rifting of the Izu arc, as well as regional-scale rifting of the Tonga–Kermadc arc at 6–3 Ma (Gill et al., 1992; Clift and ODP Leg 135 Scientific Party, 1995). Silicic calderas in the western Aleutian arc (Miller, 1995) are localized at the extensional, trailing edges of rotating crustal blocks formed by oblique subduction (Geist et al., 1988). Localized extension of the central segment of the New Hebrides arc (with six silicic calderas) is controlled by subduction of an extinct arc (Greene et al., 1988), and caldera formation in the Kermadec arc has been attributed to localized intra-arc extension along rifts that emanate obliquely from the Havre Trough backarc basin into the volcanic front (Worthington et al., 1999). We cannot unequivocally prove which, if any, of these scenarios apply to the Alisitos arc, because the 60 km long Rosario segment described here is the only part of the 300 km long terrane whose primary stratigraphic and structural characteristics are known. We favor the regional arc rift model, however, because there is strong evidence for extension across the entire upper plate of the Baja subduction margin at this time, and because silicic volcanic rocks appear to be common along the length of the arc (Busby, 2004). Additionally, none of the modern examples of localized oceanic arc extension have the abundant mafic volcanic rocks and dikes that we describe here for phase 2 (time slice 4, Fig. 7), but they typify the <2 my old Simisu rift (Izu–Bonin arc), and are considered precursory to spreading center magmatism (see summary in Marsaglia, 1995).

A puzzling aspect of the silicic volcanic rocks in the Alisitos arc is that nearly all of the subaerial ignimbrites are densely welded, and some are high-grade ignimbrites (Figs. 2–4; Table 1). The closest analog to these may lie in the Aeolian arc, which is also extensional; future petrogenetic studies in the Alisitos arc may resolve this question.

The silicic lava dome that grew on the south margin of the subaerial edifice appears to cover

more time than is typical of lava domes, since it interfingers with strata of 1, 2 and early 3 (Fig. 7), forming a very thick deposit (~3 km thick and ~6 km long, Fig. 2). In these ways it is similar to the polygenetic lava dome that forms the Mammoth Mountain ski area, where a Sierra Nevada frontal fault intersects the edge of the Long Valley caldera, and repeatedly taps into the magma body below it (Bailey, 1989). The very close proximity and similar mineralogy between the dome complex and the La Burra granite suggests a genetic relationship that could be tested geochemically. This raises the possibility that there was fault control on the siting of this dome complex, and that the fault was obliterated by intrusions of the silicic dome complex or the pluton of San Fernando (Figs. 2, 5, 7). If a fault controlled the siting of the dome complex, no faults with significant throw cut strata above the dome complex, although minor down-to-the-south normal faults do cut them (Figs. 4, 5). Strata that interfinger with the dome complex on either side of it appear to be downdropped southward into the marine basin to the south (e.g., tuff of Aguajito), but this apparent displacement could be explained by paleotopographic effects on the southern flank of the subaerial edifice.

The NE–SW orientation of dikes and the major syndepositional faults is roughly perpendicular to the modern-day trend of the 400×30 km outcrop belt of the Alisitos arc. One could argue that the apparent cross faults represent a relay ramp between two en echelon rift segments, but that does not explain the orientation of the widespread dikes. One possibility is that the Rosario segment was rotated 90° before or during backarc basin closure. A second alternative is that this segment formed at a bend in the arc, similar to faults and grabens that lie orthogonal to the trench at the southern end of the Marinas arc (Fryer et al., 1998). Volcanoes and presumably dikes follow these cross faults, inferred to form by radial expansion (Fryer et al., 1998). The large amount of extension in such a setting (Fryer et al., 1998) is consistent with our interpretation of high tectonic subsidence rates for the Rosario segment of the Alisitos arc.

Mapping is needed in other parts of the Alisitos arc to determine regional-scale structural controls on tectonic subsidence of the Rosario segment. Photic-zone rudist reefs accumulated along the southern margin of the subaerial edifice throughout deposition of the >3 km thick section, in less than 1.5 MY, requiring very high tectonic subsidence rates of about 2 km/MY. Abundant dikes, as well as numerous normal faults with small displacements, accommodated a small amount of extension, but the Rosario segment contains only one normal fault zone with major throw (the possible cross fault, described above). It is tempting to use westward flattening of stratal dips to infer fanning toward an east-dipping normal fault now covered by younger sedimentary rocks to the west; however, these attitudes are likely a product of shortening during accretion, since folds tighten dramatically from west to east (Fig. 2). Diffuse extension during early rifting produced a ~100-km zone with several tilted blocks of island-arc crust in the northern Mariana trough (Yamazaki and Murakami, 1998); the area described in detail in this paper could fit within one of those tilted blocks.

The weakness and thinness of island arc lithosphere allows for more rapid rifting than is possible in a continental rift setting, although continental arcs may rift nearly as quickly (Yamazaki and Murakami, 1998). Some workers in modern rifted oceanic arcs have proposed that rift propagation takes more than 5 MY (Tamaki et al., 1992; Taylor, 1992), but more recent studies have shown it takes less than 3 MY (Yamazaki and Murakami, 1998). Thus, the entire upper crustal section described here, which formed in less than 1.5 MY, could have been generated by the rifting process.

Regional field and geochronological data (summarized by Busby, 2004) indicate that the Alisitos arc was accreted to the western edge of Mexico by underthrusting along high-angle reverse faults at about 105 Ma. The rifting event we have dated at 110–111 Ma in the Rosario segment therefore could not have produced much, if any, backarc sea floor. In fact, ductile deformation of plutons elsewhere in the arc (Johnson et al., 1999) indicates that the middle crust was still hot when the arc was accreted. An analogous situation is occurring today at the north end of the Izu–Bonin arc, where a rifting arc is being subducted (Suyehiro et al., 1996). This is a "hot" arc, with a thick tonalitic middle crust that is weak, and a strongly-coupled lower crust and mantle that may have been "strengthened" by mafic rift intrusions (Suyehiro et al., 1996; Takahashi et al., 1998; Boutelier et al., 2003). A thick arc crust is more likely to

accrete than a thin one, but experiments show that the existence of any weak layer within the arc, regardless of arc thickness, favors accretion of the upper (felsic) crust while the lower (mafic and ultramafic) crust can be subducted (Boutelier et al., 2003). Delamination like that proposed for the Izu–Bonin collisional zone (Soh et al., 1998; Nitsuma, 1999) may explain the lack of apparent lower crustal and ultramafic rocks in the Alisitos arc terrane. This process has fundamental significance for the growth of continental crust (Suyehiro et al., 1996; Takahashi et al., 1998; Taira et al., 1998). We suggest that accretion of the Alisitoc arc by this process contributed substantially to the growth of the Mexican continental margin.

7. Conclusions

The Alisitos arc is an oceanic arc that formed in an extensional strain regime, and probably fringed North America. Evidence for arc extension and rifting include syndepositional normal faults, very high subsidence rates, debris avalanche deposits, and silicic calderas, culminating in widespread basaltic volcanism. Very detailed mapping of an intact upper crustal section (Rosario segment) allows us to divide the tectonstratigraphic and magmatic evolution of this oceanic arc terrane into two phases: (I) extensional oceanic arc, which includes 1–3, and (II) rifted oceanic arc, consisting of time slice 4 (Fig. 7). U–Pb zircon dates on volcanic and plutonic rocks show that both phases spanned less than 1.5 MY, and photic-zone sedimentation throughout this history requires very high tectonic subsidence rates of about 2 km/MY.

During both the extensional arc phase and the arc rifting phase, the Rosario segment was subaerial around a main eruptive center, which was flanked by contrasting basin types: a fault-bounded, deep-marine basin to the present-day north, and a volcano-bounded, shallow- to deep-marine basin to the present-day south. Distinctive characteristics of these two basin types in the Alisitos arc can be used to distinguish volcano-bounded and fault-bounded intra-arc basins in other settings. We recognize two types of units that are widespread enough to permit tentative stratigraphic correlation for distances of >100: a welded dacite ignimbrite erupted from La Burra caldera, and a deepwater debris-avalanche deposit.

Phase 1 (extensional oceanic arc, 1–3, Fig. 7) records processes that occur in on oceanic arc when they just beginning to “unzip”. Rifting of an oceanic arc and the resultant change in stress regime produces silicic calderas, and the La Burra caldera is the most prominent feature of the Rosario segment of the Alisitos arc. During phase 1, the two types marine basins that flanked the subaerial edifice contrasted in the following ways:

(1) Tuff turbidites are more common than pyroclastic flow deposits in the fault-bounded basin than they are in the volcano-bounded basin; this is because pyroclastic flows disintegrated into turbulent suspensions that mixed with water when they traversed the rugged, fault-controlled margin of the northern basin.
(2) Volcanism within the volcano-bounded basin was limited to small-volume nonexplosive eruptions at central vents. In contrast, the fault zone at the margin of the northern basin plumbed larger volumes of magma to the surface, producing a silicic pyroclastic caldera and associated hypabassyal intrusions, as well as silicic fire fountain deposits.
(3) Slumping and other mass wasting events were rare and small in scale in the volcano-bounded basin relative to the fault-bounded basin, where topography was steeper and seismicity more common.
(4) Rudist bioherms and associated bioclastic turbidite aprons are well-developed in the volcano-bounded basin, and absent in the fault-bounded basin. This is because steeper, unstable slopes on the margin of the fault-bounded basin were unfavorable to the development of bioherms. Rare beach conglomerates are also restricted to the volcano-bounded basin.

Phase II (rifted oceanic arc, time slice 4, Fig. 7) records an outpouring of basalts and emplacement of associated dike swarms. Silicic hypabyssal intrusions and welded tuff are also present, but intermediate-composition volcanic rocks are restricted to a single lava flow. The southern, volcano-bounded marine basin and the northern, fault-bounded marine

basin differed in two important ways during arc rifting:

(1) Volcanism in the volcano-bounded basin was centered at one vent, with a range of compositions. In contrast, volcanism in the fault-bounded basin was noncentralized, and wholly mafic, with abundant dike–sill complexes feeding eruptive equivalents. This suggests that faulting of the northern basin provided multiple unhindered conduits for the ascent of mafic magma.
(2) Volcanic cones grew above sea level within the volcano-bounded basin during phase 2, while vents remained deeply submerged in the fault-bounded basin. This indicates that subsidence in the fault-bounded basin outpaced rapid aggradation of basalt lavas and volcaniclastic rocks during arc rifting.

We propose that accretion of the oceanic arc was accomplished by detachment of the upper crust along a still hot, thick middle crustal tonalitic layer, similar to that described for the Izu–Bonin arc during subduction of mafic–ultramafic substrate. This process contributed substantially to the growth of the continent.

Acknowledgement

This research was supported by National Science Foundation Grant EAR-93-04130 and an American Chemical Society Petroleum Research Fund Grant, both to C. Busby. Formal reviews by Peter Clift and James White and earlier reviews by Richard Fisher and James Kennett were valuable. We are thankful for discussions with Eric Baer, Kari Bassett, Lars Blikra, Ben Kneller, Peter Kokelaar, Jean-Luc Schneider, and Shinji Takarada. The first author thanks her oldest daughter Claire for braving attacks from the leaping cactus on 15 mile cross-canyon hikes when she was only eight years old. The graphic art wizardry of Dottie McLaren is gratefully acknowledged.

References

Allen, P.A., 1997. Earth Surface Processes. Blackwell Science, Oxford. 404 pp.

Allison, E.C., 1955. Middle Cretaceous gastropoda of Punta China, Baja California, Mexico. Journal of Paleontology 29, 400–432.

Allison, E.C., 1974. The type Alisitos Formation (Cretaceous, Aptian–Albian) of Baja California and its bivalve fauna. In: Gastil, R.G. (Ed.), Geology of Peninsular California: Guidebook. Pacific Section S.E.P.M., pp. 29–59.

Arculus, R.J., Gill, J.B., Cambray, H., Chen, W., Stern, R., 1995. Geochemical evolution of arc systems in the western Pacific: the ash and turbidite record recovered by drilling. In: Taylor, B., Natland, J. (Eds.), Active Margins and Marginal Basins of the Western Pacific. American Geophysical Union, Geophysical Monograph, vol. 88, 45–66.

Bailey, R.A., 1989. Quaternary Volcanism of Long Valley Caldera, and Mono-Inyo Craters, Eastern California: 28th International Geological Congress, Field trip Guidebook T313. American Geophysical Union, Washington, DC. 36 pp.

Bassett, K., Busby, C., 2005. Structure and tectonic setting of an intra-arc strike-slip basin (Bisbee Basin, Southern Arizona). In: Anderson, T.H., Nourse, J.A., McKee, J.W., Steiner, M.B. (Eds.), The Mojave-Sonora Megashear Hypothesis: Development, Assessment, and Alternatives. Geological Society of America Special Paper, vol. 393.

Beggs, J.M., 1984. Volcaniclastic rocks of the Alisitos Group, Baja California, Mexico. In: Frizzell, V.A. (Ed.), Geology of the Baja California Peninsula, Book, vol. 39. Pacific Section Society Economic Paleontologists and Mineralogists, Los Angeles, pp. 43–52.

Beggs, J.M., 1984. Volcaniclastic rocks of the Alisitos Group, Baja California, Mexico. In: Frizzell, V.A. (Ed.), Geology of the Baja California Peninsula, Book, vol. 39. Pacific Section Society Economic Paleontologists and Mineralogists, Los Angeles, pp. 43–52.

Bloomer, S., Stern, R., Smoot, C., 1989. Physical volcanology of the submarine Mariana and volcano arcs. Bulletin of Volcanology 51, 210–224.

Bloomer, S.H., Stern, R.J., COOK 17 Shipboard Party, 2001. Mantle inputs to the subduction factory: detailed studies of the southern Mariana seamount province. EOS Transactions - American Geophysical Union 82 (47), F1201–F1202 (Fall Meeting Suppl.).

Branney, M.J., Kokelaar, P., 1992. A reappraisal of ignimbrite emplacement; progressive aggradation and changes from particulate to non-particulate flow during emplacement of high-grade ignimbrite. Bulletin of Volcanology 54, 504–520.

Boutelier, D., Chemenda, A., Burg, J.-P., 2003. Subduction versus accretion of intra-oceanic island arcs: insight from thermo-mechanical analogue experiments. Earth and Planetary Science Letters 212, 31–45.

Bridges, N.T., 1997. Ambient effects on basalt and rhyolite lavas under Venusian, subaerial and subaqueous conditions. Journal of Geophysical Research 102, 9243–9255.

Busby, C.J., 2004. Continental growth at convergent margins facing large ocean basins: a case study from Mesozoic convergent-margin basins of Baja California, Mexico. Tectonophysics 392, 241–277.

Busby, C.J., 2005. Possible distinguishing characteristics of very deepwater explosive and effusive silicic volcanism. Geology 33 (11), 845–848.

Busby, C.J., Rood, D., Wagner, D., 2003. Tertiary Volcanic Stratigraphy and Structure of the Sonora Pass Region, vol. 84, no. 46. American Geophysical Union, Central Sierra Nevada, California, p. F1622.

Busby, C.J., Bassett, K., Steiner, M.B., Riggs, N.R., 2005. Climatic and tectonic controls on Jurassic intra-arc basins related to northward drift of North America. In: Anderson, T.H., Nourse, J.A., McKee, J.W., Steiner, M.B. (Eds.), The Mojave-Sonora Megashear Hypothesis: Development, Assessement, and Alternatives. Geological Society of America Special Paper, vol. 393, pp. 359–376.

Busby-Spera, C.J., 1986. Depositional features of rhyolitic and andesitic volcaniclastic rocks of the Mineral King submarine caldera complex, Sierra Nevada, California. Journal of Volcanology and Geothermal Research 27, 43–76.

Busby-Spera, C.J., 1988. Speculative tectonic model for the Early Mesozoic arc of the southwest Cordilleran United States. Geology 16, 1121–1125.

Busby-Spera, C.J., White, J.D.L., 1987. Variation in peperite textures associated with differing host sediment properties. Bulletin of Volcanology 49 (6), 765–776.

Cambray, H., Pubellier, M., Joliet, L., Pouclet, A., 1995. Volcanic activity recorded in deep-sea sediments and the geodynamic evolution of western Pacific island arcs. In: Taylor, B., Natlkand, J. (Eds.), Active Margins and Marginal Basins of the Western Pacific. American Geophysical Union, Geophysical Monograph, vol. 88, 97–125.

Camus, G., Gorgaud, A., Moussand-Berthommier, P.-C., Vincent, P.-M., 2000. Merapi (Central Java, Indonesia): an outline of the structural and magmalogical evolution, with a special emphasis to the major pyroclastic events. Journal Volcanology and Geothermal Research 100, 139–163.

Cas, R.A.F., 1978. Silicic lavas in Paleozoic flysch-like deposits in New South Wales, Australia: behavior of deep silicic flows. Geological Society of America Bulletin 89, 1708–1714.

Cas, R.A.F, Yamagishi, H.M., Moore, L., Scutter, C., 2003. Miocene submarine fire fountain deposits, Ryugazaki Headland, Oshoro Penninsula, Hokkaido, Japan: implications for submarine fire fountain dynamics and fragmentation processes. In: White, J., Smellie, J., Clague, D. (Eds.), Explosive Subaqueous Volcanism. American Geophysical Union, Geophysical Monograph 140, 299–316.

Centeno-Garcia, E., 2005. Review of Upper Paleozoic and Lower Mesozoic stratigraphy and depositional environments of central and west Mexico: constraints on terrane analysis and paleogeography. In: Anderson, T.H., Nourse, J.A., McKee, J.W., Steiner, M.B. (Eds.), The Mojave-Sonora Megashear Hypothesis: Development, Assessment, and Alternatives. Geological Society of America Special Paper, vol. 393, pp. 233–258.

Cioni, R., Sbrana, A., Vecci, R., 1992. Morphological features of juvenile pyroclasts from magmatic and phreatomagmatic deposits of Vesuvius. Journal Volcanology and Geothermal Research 51, 61–78.

Clague, D.A., Davis, A.S., Bischoff, J.L., Dixon, J.E., Geyer, R., 2000. Lava bubble wall fragments formed by submarine hydrovolcanic explosions on Lo'ihi seamount and Kilauea volcano. Bulletin of Volcanology 61, 437–449.

Clift, P.D., Lee, J., 1998. Temporal evolution of the Mariana arc during rifting of the Mariana Trough traced through the volcaniclastic record. The Island Arc 7, 496–512.

Clift, P.D., ODP Leg 135 Scientific Party, 1995. Volcanism and sedimentation in a rifting island-arc terrane: an example from Tonga, southwest Pacific. In: Smellie, J.L. (Ed.), Volcanism Associated with Extension at Consuming Plate Margins, Geological Society London Special Publication, vol. 81, pp. 29–51.

Clift, P.D., Hannigan, R., Blusztajn, J., Draut, A.E., 2002. Geochemical evolution of the Dras–Kohistan Arc during collision with Eurasia; evidence from the Ladakh Himalaya India. The Island Arc 11 (4), 255–273.

Clift, P.D., Schouten, H., Draut, A.E., 2003. A general model of arc-continent collision and subduction polarity reversal from Taiwan and the Irish Caledonides. In: Larter, R.D., Leat, P.T. (Eds.), Intra-Oceanic Subduction Systems; Tectonic and Magmatic Processes. Geological Society of London, Special Publication, vol. 219, pp. 81–98.

Clift, P.D., Dewey, J.F., Draut, A.E., Chew, D., Mange, M., Ryan, P.D., 2004. Rapid tectonic exhumation, detachment faulting and orogenic collapse in the Caledonides of Western Ireland. Tectonophysics 384, 91–113.

Cole, J.W., 1984. Taupo–Rotorua depression: an ensialic marginal basin of the North Island, New Zealand. Special Publication - Geological Society of London 16, 109–120.

Cole, R.B., DeCelles, P.G., 1991. Subaerial to submarine transitions in Early Miocene pyroclastic flow deposits, southern San Joaquin basin California. Geological Society of America Bulletin 103, 221–235.

Collinson, J.D., 1996. Alluvial sediments. In: Reading, H.G. (Ed.), Sedimentary Environments: Processes, Facies and Stratigraphy, 3rd ed. Blackwell Science, Oxford. 688 pp.

Crandell, D.R., Mullineaux, D.R., Sigafoos, R.S., Rubin, M., 1974. Chaos Crags eruptions and rockfall avalanches. J. Res., vol. 2. U.S. Geol. Surv., Lassen Volcanic National Park, California, pp. 49–59.

DeOreo, S., Busby, C.J., Skilling, I., 2003. Tertiary Paleogeography and Paleotectonic Evolution of the Sierra Nevada in The Carson Pass–Kirkwood Area, vol. 84, no. 46. American Geophysical Union, California, p. F1622.

Draut, A.E., Clift, P.D., 2001. Geochemical evolution of arc magmatism during arc–continent collision South Mayo, Ireland. Geology 29, 543–546.

Draut, A.E., Clift, P.D., Hannigan, R., Layne, G.D., Shimizu, N., 2002. A model for continental crust genesis by arc accretion: rare earth element evidence from the Irish Caledonides. Earth and Planetary Science Letters 203 (3–4), 861–877.

Draut, A.E., Clift, P.D., Chew, D.M., Cooper, M.J., Taylor, R.N., Hannigan, R.E., 2004. Laurentian crustal recycling in the Ordovician Grampian Orogeny: Nd isotopic evidence from western Ireland. Geological Magazine 141 (2), 195–207.

Dickinson, W.R., Lawton, T.F., 2001. Carboniferous to Cretaceous assembly and fragmentation of Mexico. Geological Society of America Bulletin 113, 1142–1160.

Eppler, D.B., Fink, J., Fletcher, R., 1987. Rheologic properties and kinematics of emplacement of the Chaos Jumbles rockfall avalanche, Lassen Volcanic National Park California. Journal of Geophysical Research 92, 3623–3633.

Fackler Adams, B.N., 1997. Volcanic and sedimentary facies, processes and tectonics of intra-arc basins: jurassic continental arc of California and Cretaceous oceanic arc of Baja California: unpublished Ph.D. thesis, University of California at Santa Barbara. 248 pp.

Fackler Adams, B.N., Busby, C.J., 1998. Structural and stratigraphic evolution of extensional oceanic arcs. Geology 26 (8), 735–738.

Fink, J.H., Anderson, S.W., 2000. Lava domes and coulees. In: Sigurdsson, H., Houghton, B.F., McNutt, S.R., Rymer, H., Stix, J. (Eds.), Encyclopedia of Volcanoes. Academic Press, New York, pp. 307–320.

Fisher, R.V., Schmincke, H.-U., 1984. Pyroclastic Rocks. Springer-Verlag, New York. 472 pp.

Fisher, R.V., Smith, A.L., Roobol, M.J., 1980. Destruction of St Pierre, Martinique, by ash-cloud surge, May 8 and 20, 1902. Geology 8, 472–476.

Fiske, R.S., 1963. Subaqueous pyroclastic flows in the Ohanapecosh Formation, Washington. Geological Society of America Bulletin 74, 391–406.

Fiske, R.S., Matsuda, T., 1964. Submarine equivalents of ash flows in the Tokiwa formation, Japan. American Journal of Science 262, 76–106.

Fiske, R.S., Naka, J., Iizasa, K., Yuasa, M., 1995. Caldera-forming submarine pyroclastic eruption at Myojin Knoll, Izu–Bonin Arc. JAMSTEC Journal of Deep Sea Research 11, 315–322.

Freundt, A., 1999. Formation of high-grade ignimbrites: Part II. A pyroclastic suspension current model with implications also for low-grade ignimbrites. Bulletin Volcanologique 60, 545–567.

Freundt, A., Wilson, C.J.N., Carey, S.N., 2000. Ignimbrites and block-an-ash flow deposits. In: Sigurdsson, H. (Ed.), Encyclopoedia of Volcanoes. Academic Press, San Diego, pp. 581–600.

Fryer, P., 1996. Evolution of the Mariana convergent plate margin system. Reviews of Geophysics 34, 89–125.

Fryer, P., Fujimoto, H., Sekine, M., Johnson, L.E., Kasahara, J., Masuda, H., Gamo, T., Ishii, T., Ariyoshi, M., Fujioka, K., 1998. Volcanoes of the southwestern extension of the active Mariana island arc: new swath-mapping and geochemical studies. The Island Arc 7, 596–607.

Fujibayashi, N., Sakai, U., 2003. Vesiculation and eruption processes of submarine effusive and explosive rocks from the Middle Miocene Ogi Basalt, Sado Island, Japan. In: White, J., Smellie, J., Clague, D. (Eds.), Explosive Subaqueous Volcanism, Geophysical Monograph Series, vol. 140. American Geophysical Union, pp. 259–272.

Galloway, W.E., 1989. Genetic stratigraphic sequences in basin analysis: I. Architecture and genesis of flooding-surface bounded depositional units. American Association Petroleum of Geologists Bulletin 73 (2), 125–142.

Gastil, R.G., Phillips, R.C., Allison, E.C., 1975. Reconnaissance geology of the state of Baja California. Memoir - Geological Society of America 140 (170 pp.).

Geist, E.L., Childs, J.R., Scholl, D.W., 1988. The origin of summit basins of the Aleutian Ridge: implications for block rotations of an arc massif. Tectonics 7, 327–341.

Gibson, H.L., Morton, R.L., Hudak, G.J., 2000. Submarine volcanic processes, deposits and environments favorable for the location of volcanic-hosted massive sulfide deposits. In: Barrie, C.T., Hannington, Mark D. (Eds.), Volcanic-Associated Massive Sulfide Deposits: Processes and Examples in Modern and Ancient Settings, Reviews in Economic Geology, vol. 8, pp. 13–51.

Gill, J., et al., 1990. Explosive deep water basalts in the Simisu backarc rift. Science 248, 1214–1217.

Gill, J.B., Seales, C., Thompson, P., Hoichstaedter, A.G., Dunlap, C., 1992. Petrology and geochemistry of Pliocene–Pleistocene volcanic rocks from the Izu arc, Leg 126. In: Taylor, B., Fujioka, K. (Eds.), Proceedings Ocean Drilling Project, Scientific Results, vol. 126, pp. 383–404.

Giordano, G., De Rita, D., Cas, R., Rodani, S., 2002. Valley pond and ignimbrite veneer depositd in the small-volume phreatomagmatic "Perino lbano" basic ignimbrite, Lago Albano maar, Colli Albani volcano, Italy: influence of topography. Journal Volcanology and Geothermal Research 118, 131–144.

Glasby, G.P., Izasa, K., Yusa, M., Usui, A., 2000. Submarine hydrothermal mineralization on the Izu–Bonin arc, south of Japan: an overview. Marine Georesources and Geotechnology 18, 141–176.

Glicken, H., 1986. Rockslide–debris avalanche of May 18, 1980 Mount St. Helens volcano: unpubl. PhD dissertation, Univ Calif Santa Barbara. 303 pp.

Glicken, H., 1991. Sedimentary architecture of large volcanic-debris avalanches. In: Fisher, R.V., Smith, G.A. (Eds.), Sedimentation in Volcanic Settings, S.E.P.M. Special Pub., vol. 45, pp. 99–106.

Greene, H.G., Macfarlaner, A., Johnston, D.P., Crawford, A.J., 1988. Structure and tectonics of the central New Hebrides arc. In: Greene, H.G., Wong, F.L. (Eds.), Geology and Offshore Resources of Pacific Island Arcs – Vanuatu Region. CircumPacific Council Energy and Mineral Resources, Houston, Texas, pp. 377–412.

Hackett, W.R., Houghton, B.F., 1989. A facies model for Quaternary andesitic composition volcano: Ruapehu, New Zealand. Bulletin Volcanologique 51, 51–68.

Heiken, G., Wohletz, K., 1985. Volcanic Ash. University of California Press, Berkeley, California. 246 pp.

Hoffman, P.F., 1989. Precambrian geology and tectonic history of North America. In: Bally, A.W., Palmer, A.R. (Eds.), The Geology of North America — an Overview, The Geology of North America, vol. A. Geological Society of America, pp. 447–512.

Honnorez, J., Kirst, P., 1975. Submarine basaltic volcanism: morphometric parameters for discriminating hyaloclastites from hyalotuffs. Bulletin Volcanologique 34–3, 1–25.

Houghton, B.F., Wilson, C.J.N., Pyle, D.M., 2000. Pyroclastic fall deposits. In: Sigurdsson, H., Houghton, B.F., McNutt, S.R., Rymer, H., Stix, J. (Eds.), Encyclopedia of Volcanoes. Academic Press, New York, pp. 555–570.

Houghton, B.F., Wilson, C.J.N., Smith, R.T., Gilbert, J.S., 2000. Phreatoplinian eruptions. In: Sigurdsson, H., Houghton, B.F.,

McNutt, S.R., Rymer, H., Stix, J. (Eds.), Encyclopedia of Volcanoes. Academic Press, New York, pp. 513–526.

Izasa, K., Fiske, R.S., Ishizuka, O., Yuasa, M., Hshimoto, J., Naka, J., Horii, Y., Fujiwara, Y., Imai, A., Koyama, S., 1999. A Kuroko-type polymetallic sulfide deposit in a submarine silicic caldera. Science 283, 975–977.

Johnson, S., Tate, M.C., Fanning, C.M., 1999. New geologic mapping and SHRIMP U–Pb zircon data in the Peninsular Ranges batholith, Baja California: evidence for a suture? Geology 27 (8), 743–746.

Kano, K., Orton, G.J., Kano, T., 1994. A hot Miocene subaqueous scoria deposit in the Shiname Peninsula, SW Japan. Journal of Volcanology and Geothermal Research 60, 1–14.

Kasuga, S., Kato, Y., 1992. Discovery of hydrothermal ore deposits in the crater of the Suiyo Seamount on the Izu–Ogasawara arc. Proc. JAMSTEC Symp. Deep Sea Research, pp. 249–255 (in Japanese with English abstract).

Kerr, D.R., Abbott, P.L., 1996. Miocene subaerials turzstrom deposits Split Mountain, Anza–Borego Desert Park. In: Abbott, P.L., Seymour, D.C. (Eds.), Sturzstroms and Detachment Faults, Anza–Borego Desert State Park, California. Sout Coast Geological Society, Santa Ana, California, pp. 149–163.

Klaus, A., Taylor, B., Moore, G., MacKay, M., Okamura, Y., an Murakami, F., 1992. Structural and stratigraphic evolution of the Sumisu Rift, Izu–Bonin arc. In: Taylor, B., Fujioka, K., Janacek, T., Langmuir, C. (Eds.), Proceedings of the Ocean Drilling Program, Scientific Results, Leg 126, pp. 555–573.

Kokelaar, B.P., Busby, C.J., 1992. Subaqueous explosive eruption and welding of pyroclastic deposits. Science, Full Article 257, 196–201.

Kokelaar, P., Romagnoli, C., 1995. Sector collapse, sedimentation and clast population evolution at an active island-arc volcano: Stromboli, Italy. Bulletin of Volcanology 57, 240–262.

Larsen, J.F., Nye, C.J., Ray, L.A., 2000. The 2050 BP Okmok Caldera forming event: evidence for magma mixing as an eruption trigger [abs.]. Eos 81 (48), 1376.

Lenat, J.F., Vincent, P., Bachelery, P., 1989. The offshore continuation of an active basaltic volcano: piton de la Fournaise (Reunion Island, Indian Ocean): structural and geomorphological interpretation from Seabeam mapping. Journal of Volcanology and Geothermal Research 36, 1–36.

Lloyd, E.F., Nathan, S., 1981. Geology and tephrachronology of Raoul Island, Kermadec Group, New Zealand. New Zealand Geological Survey Bulletin, vol. 95 Wellington. 105 pp.

Lloyd, E.F., Nathan, S., Smith, I.E.M., Stewart, R.B., 1996. Volcanic history of Macauley Island, Kermadec Ridge, New Zealand. New Zealand Journal of Geology and Geophysics 39, 295–308.

Lowe, D.R., 1982. Sediment gravity flows II: depositional models with special reference to the deposits of high density turbidity currents. Journal of Sedimentary Geology 52, 279–297.

Ludwig, K.J., 2001. Isoplot/Ex (rev. 2.49). Berkeley Geochronology Center Special Publication, vol. 1a. 56 pp.

Marsaglia, K.M., 1995. Interarc and backarc basins. In: Busby, C.J., Ingersoll, R.V. (Eds.), Tectonics of Sedimentary Basins. Blackwell Science, Cambridge Massachusetts, pp. 299–330.

Mattinson, J.M., 1994. A study of complex discordance in zircons using step-wise dissolution techniques. Contributions to Mineralogy and Petrology 116, 117–129.

Mattinson, J.M., 1997. Analysis of zircons By Multi-Step Partial Dissolutions: The Good, The Bad, and The Ugly: GAC/MAC Ottawa '97 Abst. Vol. A98.

Mattinson, J.M., 2003. CA (chemical abrasion) – TIMS: high-resolution U–Pb zircon geochronology combining high-temperature annealing of radiation damage and multi-step partial dissolution analysis. EOS Transactions AGU 84 (46) (Fall Meeting Suppl., Abstract V22E-06).

Mattinson, J.M., 2005. Zircon U–Pb chemical abrasion ("CA-TIMS") method: combined annealing and multi-step partial dissolution analysis for improved precision and accuracy of zircon ages. Chemical Geology 220, 47–66.

McBirney, A.R., Murase, T., 1984. Rheological properties of magmas. Annual Review of Earth and Planetary Sciences 12, 337–357.

McCurray, M., Watkins, K., Parker, J., Wright, K., Hughes, S., 1996. Preliminary volcanological constraints for sources of high-grade, rheomorphic ignimbrites of the Cassia Mountains, Idaho: implications for the evolution of the Twin Falls volcanic center. In: Hughes, S., Thomas, R. (Eds.), 21st Annual Field Conference of the Tobacco Root Geological Society, Twin Falls, Northwest Geology, vol. 26, pp. 81–91.

McCurry, M., Schmidt, K., 2001. Petrology and oxygen isotope geochemistry of the Pucon Ignimbrite — Southern Andean Volcanic Zone, Chile: implications for genesis of mafic ignimbrites: III. South American symposium on isotope geology, Extended Abstracts Volume (CD), Sociedad Geologica de Chile, Santiago, Chile, pp. 317–320.

McPhie, J., Doyle, M., Allen, R., 1993. Volcanic Textures: a Guide to the Interpretation of Textures in Volcanic Rocks: Center for Ore Deposit and Exploration Studies. University of Tasmania. 196 pp.

Miller, T.P., 1995. Late Quaternary caldera formation along the Aleutian arc: distribution, age and volume. EOS Transactions - American Geophysical Union 76, 680.

Monzier, M., Robin, C., Eissen, J.-P., 1994. Kuwae (~1425 A.D.): the forgotten caldera. Journal of Volcanology and Geothermal Research 59, 207–218.

Moore, J.G., Normark, W.R., Holcomb, R.T., 1994. Giant Hawaiian landslides. Annual Review of Earth and Planetary Sciences 22, 119–144.

Morissey, M., Zimanowski, B., Wohletz, K., Buettner, R., 2000. Phreatomagmatic fragmentation. In: Sigurdsson, H., Houghton, B.F., McNutt, S.R., Rymer, H., Stix, J. (Eds.), Encyclopedia of Volcanoes. Academic Press, New York, pp. 431–446.

Mueller, W., White, J.D.L., 1992. Felsic fire-fountaining beneath Archean seas: pyroclastic deposits of the 2730 Ma Hunter Mine Group, Quebec, Canada. Journal of Volcanology and Geothermal Research 54, 117–134.

Murakami, F., 1996. Seismic stratigraphy and structural characteristics of back-arc rifts on the Izu–Ogasawara Arc. The Island Arc 5, 25–42.

Naka, J., Fiske, R.S., Taira, A., Yamamoto, F., IIizasa, K., Yuasa, M., 1995. Geology of Myojin Knoll, Izu–Bonin Arc, Japan.

JAMSTEC Journal of Deep Sea Research, 127–137 (in Japanese with English abstract).

Nishimura, A., Rodolfo, K., Koizumi, A., Gill, J.B., Fujioka, K., 1992. Episodic deposition of Pliocene–Pleistocene pumice deposits of the Izu–Bonin Arc. In: Taylor, B., Fujioka, K., Janecek, T., Langmuir, C. (Eds.), Proceedings of the Ocean Drilling Program, Scientific Results, Leg 126. Ocean Drilling Program, College Station, Texas, pp. 3–21 Bonin Arc–Trench System, Leg 126, Sites 787–793.

Nitsuma, N., 1999. Rupture and delamination of arc crust due to the arc–arc collision in the South Fossa Magna, central Japan. The Island Arc 8, 441–458.

Palmer, B.A., Alloway, B.V., Neall, V.E., 1991. Volcanic debris avalanche deposits in New Zealand— lithofacies organization in unconfined wet avalanche flows. In: Fisher, R.V., Smith, G.A. (Eds.), Sedimentation in Volcanic Settings, S.E.P.M. Special Publication, vol. 45, pp. 89–98.

Rittman, A., 1962. Volcanoes and their Activity. John Wiley and Sons, New York. 305 pp.;
Robin, C., Eissen, J.-P., Monzier, M., 1993. Giant tuff cone and 12-km-wide associated caldera at Ambrym Volcano (Vanatu, New Hebrides Arc). Journal of Volcanology and Geothermal Research 55, 225–238.

Schmidt, K.L., Wetmore, P.H., Johnson, S.E., Paterson, S.R., 2002. Controls on orogenesis along an ocean–continent margin transition in the Jura–Cretaceous Peninsular Ranges Batholith. Special Paper — Geological Society of America 365, 49–71.

Schmincke, H.-U., Swanson, D.A., 1967. Laminar viscous flowage structures in ash-flow tuffs from Gran Canria, Canary islands. Journal of Geology 75, 641–644.

Self, S., 1983. Large scale phreatomagmatic silicic volcanism: a case study from New Zealand. Journal Volcanology and Geothermal Research 17, 433–469.

Siebe, C., Komorowski, J.C., Sheridan, M.F., 1992. Morphology and emplacement of an unusual debris-avalanche deposit at Jocotilan volcano, Central Mexico. Bulletin of Volcanology 54, 573–589.

Siebert, L., Beget, J.E., Glicken, H., 1995. The 1883 and late prehistoric eruptions of Augustine volcano, Alaska. In: Ida, Y., Voight, B. (Eds.), Models of Magmatic Processes and Volcanic Eruptions, J. Volcanol. Gepth. Res., vol. 66, pp. 367–395.

Simpson, K., McPhie, J., 2001. Fluidal-clast breccia generated by submarine fire fountaining, Trooper Creek Formation, Queensland, Australia. Journal of Volcanology and Geothermal Research 109, 239–271.

Smith, T.L., Batiza, R., 1989. New field and laboratory evidence for the origin of hyaloclastite flows on seamount summits. Bulletin of Volcanology 51, 96–114.

Smith, G.A., 1994. Intra-arc basins. In: Busby, C.J., Ingersoll, R.V. (Eds.), Tectonics of Sedimentary Basins. Blackwell Science, pp. 263–298.

Smith, G.A., Lowe, D.R., 1991. Lahars: volcano-hydrologic events and deposition in the debris flow–hyperconcentrated flood flow continuum. In: Fisher, R.V., Smith, G.A. (Eds.), Sedimentation in Volcanic Settings, SEPM (Society for Sedimentary Geology) Special Publication, vol. 45, pp. 59–70.

Soh, W., Nakayama, K., Kimura, T., 1998. Arc–arc collision in the Izu collision zone, central Japan, deduced from the Ashigara Basin and adjacent Tanzawa Mountains. The Island Arc 7, 330–341.

Sparks, R.S.J., 1997. Causes and consequences of pressurization in lava dome eruptions. Earth and Planetary Science Letters 150, 177–189.

Sparks, R.S.J., Self, S., Walker, G.P.L., 1973. Products of ignimbrite eruptions. Geology 1, 115–118.

Stacey, J.S., Kramers, J.D., 1975. Approximation of terrestrial lead isotope evolution by a two-stage model. Earth and Planetary Science Letters 26, 207–221.

Stewart, J.H., Gehrels, G.E., Barth, A.P., Link, P.K., Christie-Blick, N., Wrucke, C.T., 2001. Detrital zircon provenance of Mesoproterozoic to Cambrian arenites in the western United States and northwestern Mexico. Geological Society of America Bulletin 113, 1343–1356.

Suyehiro, K., Takahashi, N., Ariie, Y., et al., 1996. Continental crust, crustal underplating, and low-Q upper mantle beneath an oceanic island arc. Science 272, 390–392.

Taira, A., Saito, S., Aoike, K., Morita, S., Tokuyama, H., Suyehiro, M., Kiyokawa, S., Naka, J., Klaus, A., 1998. Nature and growth rate of the Northern Izu–Bonin (Ogasawara) arc crust and their implications for continental crust formation. The Island Arc 7, 395–407.

Tagudin, J.E., Scholl, D.W., 1994. The westward migration of the Tofua volcanic arc toward Lau Basin: SOPAC Technical Bulletin. In: Stevenson, A.J., et al., (Eds.), Geology and Submarine Resources Of The Tonga–Lau–Fiji Region, vol. 8, pp. 121–129.

Takahashi, N., Suyehiro, K., Shinohara, M., 1998. Implications from the seismic crustal structure of the northern Izu–Bonin arc. The Island Arc 7, 383–394.

Tamaki, K., Suyehiro, K., Allan, J., Ingle Jr., J.C., Pisciooto, K.A., 1992. Tectonic synthesis and implications of Japan Sea ODP drilling. Proceedings of the Ocean Drilling Program. Scientific Results 127/128 (pt. 2), 1333–1348.

Tappin, D.R., 1994. The Tonga frontal-arc basin. In: Balance, P.F. (Ed.), South Pacific Sedimentary Basins. Elsevier, Amsterdam, pp. 157–176.

Taylor, B., 1992. Rifting and the volcano-tectonic evolution of the Izuã Boninã Mariana arc. In: Taylor, B., Fujioka, K., Janecek, T., Langmuir, C. (Eds.), Proceedings of the Ocean Drilling Program, Scientific Results, Leg 126. Ocean Drilling Program, College Station, Texas, pp. 627–651.

Taylor, B., Brown, G., Fryer, P., Gill, J.B., Hochstaedter, A.G., Hotta, H., Langmuir, C.H., Leinen, M., Nishimura, A., Urabe, T., 1990. ALVIN-Sea Beam studies of the Sumisu Rift, Izu–Bonin Arc. Earth and Planetary Science Letters 100, 127–147.

Taylor, B., Klaus, A., Brown, G.R., Moore, G.F., Okamura, Y., Murakami, F., 1991. Structural development of Sumisu Rift, Izu–Bonin Arc. Journal of Geophysical Research 96, 16113–16129.

Ui, T., Takarada, S., Yoshimoto, M., 2000. Debris avalanches. Encyclopedia of Volcanology, pp. 617–626.

Vallance, J.W., 2000. Lahars. In: Sigurdsson, H., Houghton, B.F., McNutt, S.R., Rymer, H., Stix, J. (Eds.), Encyclopedia of Volcanoes. Academic Press, New York, pp. 601–616.

van Wagoner, J.C., Posamentier, H.W., Mitchum Jr., R.M., Vail, P.R., Sraq, J.F., Loutit, T.S., Hardenbol, J., 1988. An overview of the fundamentals of sequence stratigraphy and key definitions. In: Wilgus, C.K., Hastings, B.S., Ross, C.A., Posamentier, H.W., van Wagoner, J., Kendall, C.G. St.C. (Eds.), Sea-Level Changes; an Integrated Approach, SEPM Special Publication, vol. 42. SEPM (Society for Sedimentary Geology), Tulsa, OK, USA, pp. 39–44.

Voight, B., Glicken, H., Janda, R.J., Douglass, P.M., 1981. Catastrophic rockslide avalanche of May 18. The 1980 Eruption of Mount St. Helens, Washington, U.S.G.S. Prof. Paper, vol. 1250, pp. 47–378.

Wadge, G.P.W., Francis, P.W., Ramirez, C.F., 1995. The Socompa collapse and avalanche event. Journal of Volcanology and Geothermal Research 66, 309–336.

White, J.D.L., 2000. Subaqueous eruption-fed density currents and their deposits. Precambrian Research 101, 87–109.

White, J.D.L., Busby-Spera, C.J., 1987. Deep marine arc apron deposits and syndepositional magmatism in the Alisitos Group at Punta Cono, Baja California, Mexico. Sedimentology 34 (5), 911–927.

White, J.D.L., Smellie, J.L., Clague, D.A., 2003. Introduction. In: White, J., Smellie, J., Clague, D. (Eds.), Explosive Subaqueous Volcanism, Geophysical Monograph Series, vol. 140. American Geophysical Union, pp. 1–24.

Wilson, C.J.N., Houghton, B.F., McWilliams, M.O., Lanphere, M.A., Weaver, S.D., Briggs, R.M., 1995. Volcanic and structural evolution of Taupo Volcanic Zone, New Zealand; a review. Journal of Volcanology and Geothermal Research 68, 1–28.

Wolff, J.A., Wright, J.V., 1981. Rheomorphism of welded tuffs. Journal of Volcanology and Geothermal Research 10, 13–34.

Worthington, T.J., Gregory, M.R., Bondarenko, V., 1999. The Denham caldera on Raoul Volcano: dacitic volcanism in the Tonga–Kermadec arc. Journal of Volcanology and Geothermal Research 90, 29–48.

Wright, I.C., 1996. Volcaniclastic processes on modern submarine arc stratovolcanoes: sidescan and photographic evidence from the Rumble IV and V volcanoes, southern Kermadec Arc (SW Pacific). Marine Geology 136, 21–39.

Wright, I.C., Gamble, J.A., 1999. Southern Kermadec submarine caldera formation by effusive and pyroclastic eruption. Marine Geology 161, 207–227.

Wright, I.C., de Ronde, C.E.J., Faure, K., Gamble, J.A., 1998. Discovery of hydrothermal sulfide mineralization from southern Kermadec arc volcanoes (SW Pacific). Earth and Planetary Science Letters 164, 335–343.

Wright, I.C, Gamble, J.A., Shane, P.A.R., 2003. Submarine silicic volcanism of the Healy caldera, southern Kermadec arc (SW Pacific): 1—volcanology and eruption mechanisms. Bulletin of Volcanology 65, 15–29.

Yamagishi, H., 1987. Studies on the Neogene subaqueous lavas and hyaloclastites in southwest Hokkaido. Report of the Geological Survey of Hokkaido 59 (117 pp.).

Yamagishi, H., Dimroth, E., 1985. A comparison of Miocene and Archean rhyolite hyaloclastites: evidence for a hot and fluidal rhyolite lava. Journal of Volcanology and Geothermal Research 23, 337–355.

Yamazaki, T., Murakami, F., 1998. Asymmetric rifting of the northern Mariana trough. The Island Arc 7, 460–470.

Yuasa, M., 1995. Myojin Knoll, Izu–Ogasawara arc: submersible study of submarine pumice volcano. Bulletin of the Volcanology Society of Japan 40, 277–284 (in Japanese with English abstract).

Yuasa, M., Kano, K., 2003. Submarine silicic calderas on the northern Shichito–Iwojima Ridge, Izu–Ogasawara (Bonin) arc, western Pacific. In: White, J., Smellie, J., Clague, D. (Eds.), Explosive Subaqueous Volcanism, Geophysical Monograph Series, vol. 140. American Geophysical Union, pp. 231–244.